Additively manufactured AlSi10Mg inherently stable thin and thick-walled lattice with negative Poisson's ratio

Arun Arjunan[1], Manpreet Singh[1], Ahmad Baroutaji[1] and Chang Wang[2]

[1]School of Engineering, University of Wolverhampton, Telford Innovation Campus, Telford TF29NT, UK
[2]Department of Engineering and Design, University of Sussex, Brighton BN1 9RH, United Kingdom

Abstract

Literature on the mechanical performance of additively manufactured (AM) negative Poisson's ratio ($-\upsilon$) structures has been primarily focused on beam-based re-entrant structures with chevron crosslinks. The walled variants of this architecture have been shown to exhibit lateral instability. This is where a layered framework can be advantageous as they provide increased lateral stability. Much less is known regarding the behaviour of such architecture, let alone their thin/thick-walled variants. This study explores the influence of design parameters namely wall thickness (t) and angle (θ) on the mechanical performance of thin and thick-walled inherently stable $-\upsilon$ lattices. The design is achieved through conceiving linearly arranged AlSi10Mg re-entrant unit-cells while discarding the traditional chevron crosslinks. The printed prototypes were experimentally tested and response surface (RS) models were generated to study the parametric influence on the elastic modulus (E), compressive strength (σ_c), failure strain (ε_f), $-\upsilon$ and relative density ( ). The results demonstrate that both thin- and thick-walled structures exhibit υ of -0.108 to -0.257 despite the interaction effects between t and θ. The elastic modulus can be increased by either increasing t or θ without considering the interaction effects at $0.3 \leq t \leq 1$ mm and $45° \leq \theta \leq 85°$. This study presents a new understanding regarding the fabrication and performance of re-entrant structures by AM.

Keywords: Additive Manufacturing; Selective Laser Melting; AlSi10Mg; Thin and Thick-walled; negative Poisson's ratio

1. Introduction

When a traditional material is compressed, expansion takes place along the lateral direction to the load applied. Quantifying this phenomenon is the Poisson's ratio (υ), which is defined as the negative ratio of transverse to longitudinal strain. However, when a material deviates from the norm and gives rise to a negative Poisson's ratio ($-\upsilon$), such material can be classified auxetic [1–5]. Auxetic behaviour is receiving increasing attention due to its desirable effects such as enhanced shear modulus [6–9], resistance to impact [10–14], indentation [15–18], fracture toughness [19–22], and damping properties [23–25]. These performances then translates to applications such as novel fasteners [26,27], foams [28–34], biomedical implants [35–38] and actuators [39–41].

Though there are exceptions, widely studied 2D and 3D $-\upsilon$ structures [42–50] fall under one of the three categories namely re-entrant [51–56], chiral [57–62], and rotating rigid [63–65]. Although Additive Manufacturing (AM) allows conceiving structures that fall under any of these categories, the most studied is the re-entrant category. Other significant architectures include the anti-chiral structures studied by Alderson *et al.* [66] along with Pozniak and Wojciechowski [67] in addition to shape-preserving structures [68,69], and various composites [70,71]. Despite this, Zadpoor [72] found that studies in metals have been limited to beam-based architecture [73–76] with much less information on plate/sheet/walled/surface $-\upsilon$ architecture.

Walled variants of the re-entrant architecture exhibit average $-\upsilon$ despite allowing both lateral expansion and compression. While these structures exhibit some areas of lateral expansion, the overall behaviour is still dominated by the re-entrant architecture resulting in $-\upsilon$. As the walled variants of the traditional re-entrant architecture show significant lateral instability, the behaviour of such structures in literature are rare. Other than numerically modelled deformation of rotating rigid units [77] and kirigami paper cut structures [78], no other architecture with $-\upsilon$ has been reported. In any case, no experimental studies using metallic materials let alone additive manufactured versions have been reported. Therefore, this study provides a new impetus in the design and evaluation of AM $-\upsilon$ AlSi10Mg structure using re-entrant mechanisms combining the superior lateral stability of layered architecture.

Although some surface-based architecture can be found in literature, these are limited to non-auxetic minimal surface designs [79–82]. Moreover, recent reviews [72,83,84] make it clear that auxetic walled variants should be explored to clarify the design paradigms as they may outperform their beam counterparts. Even though beam-based re-entrant architecture allow for lateral deformation, the overall performance is driven by the global structure rather than the unit-cell [85]. Accordingly, a linearly repeating unit-cell representative of the traditional re-entrant architecture without crosslink was chosen; a methodology adopted by Li *et al.* [86] for 2D double arrowhead structure, which acts as the rationale for this study.

Numerous studies [87–96] have been dedicated to the development of $-\upsilon$ structures, out of which a large category are on mechanism modelling [97]. Studying deformation and predicting the mechanical behaviour using finite element analysis (FEA) was the approach selected in a lot of cases [45,98–106]. While this proliferates the design routes to which $-\upsilon$ can be achieved, the influence of the fundamental design parameters (t and θ) on performance is yet to be understood [107–109]. Furthermore, as observed by Yang *et al.* [76], there is a lack of agreement between numerical and experimental observations, which questions the validity of the structural behaviour where the influence of manufacturing process cannot be omitted. Considering these aspects, this study employs an experimental based design of experiments (DoE) approach to identify the influence of the design parameters and manufacturing process on $-\upsilon$. Polynomial equations are then derived to represent the respective mechanical responses that not only characterises the auxetic behaviour but also acts as design guidelines.

According to Li *et al.* [110], the most significant advantage of developing $-\upsilon$ materials are their potential to be tunable [111–113]. This allows for targeted failure strain, elastic modulus, and strength while featuring scalable unit-cells for a wide range of applications [114]. For this, the structure must be inherently stable and should feature a repeating unit-cell, while featuring fewer geometrical parameters. The thin and thick-walled $-\upsilon$ structure studied in this work satisfies these two criteria. Uzan *et al.* [115] reports that the use of AM [116–118] in conceiving cellular structures requires systematic investigation of the part quality. Simply assuming a homogenous part and characterising the mechanical response can lead to inaccurate conclusions; a case simply not considered in numerous $-\upsilon$ structures [119–121]. One of the most common AM techniques for metals is selective laser melting (SLM) [122], which is increasingly being used in the automotive [123] and space industries [124]. Accordingly, this study exploits the use of SLM to manufacture AlSi10Mg thin/thick-walled structures, where part quality is considered as part of the mechanical characterisation.

Overall, much of the research on metallic $-\upsilon$ structures have focused on beam-based designs with a few experimental studies on thin/thick-walled structures. In any case, the influence of the geometric parameters and their interaction on the mechanical performance of these structures has received no attention. This study introduces AlSi10Mg thin and thick-walled $-\upsilon$ structures allowing for an inherently stable compressive performance. Extensive physical tests advised by the DoE response surface method (RSM) were carried out to study the interaction effects of the geometrical parameters; namely wall thickness (t) and auxetic angle (θ). The elastic modulus (E), compressive strength (σ_c), failure strain (ε_f), Poisson's ratio (υ) and relative density ( ) of the structure were modelled as functions of geometrical parameters. Lastly, a parametric analysis was performed to investigate the order of significance of the geometric parameters while paying critical attention to the SLM manufacturing process. The study therefore presents a new understanding regarding the fabrication and performance of re-entrant structures by AM.

2. Material and methods

2.1. An inherently stable $-\upsilon$ architecture

The re-entrant structure is one of the most common architecture for both 2D and 3D $-\upsilon$ materials. These units tend to expand along the transverse direction when stretched and shrink when compressed [125]. For the re-entrant structure, the most common unit-cell shape is the bowtie as shown in Fig. 1a. As can be seen, this shape invariably dictates a directional auxeticity along the chevron beams when $\theta < 90°$. However, when the θ value reaches 90° or above, the structure is no longer auxetic as shown in Fig. 1b.

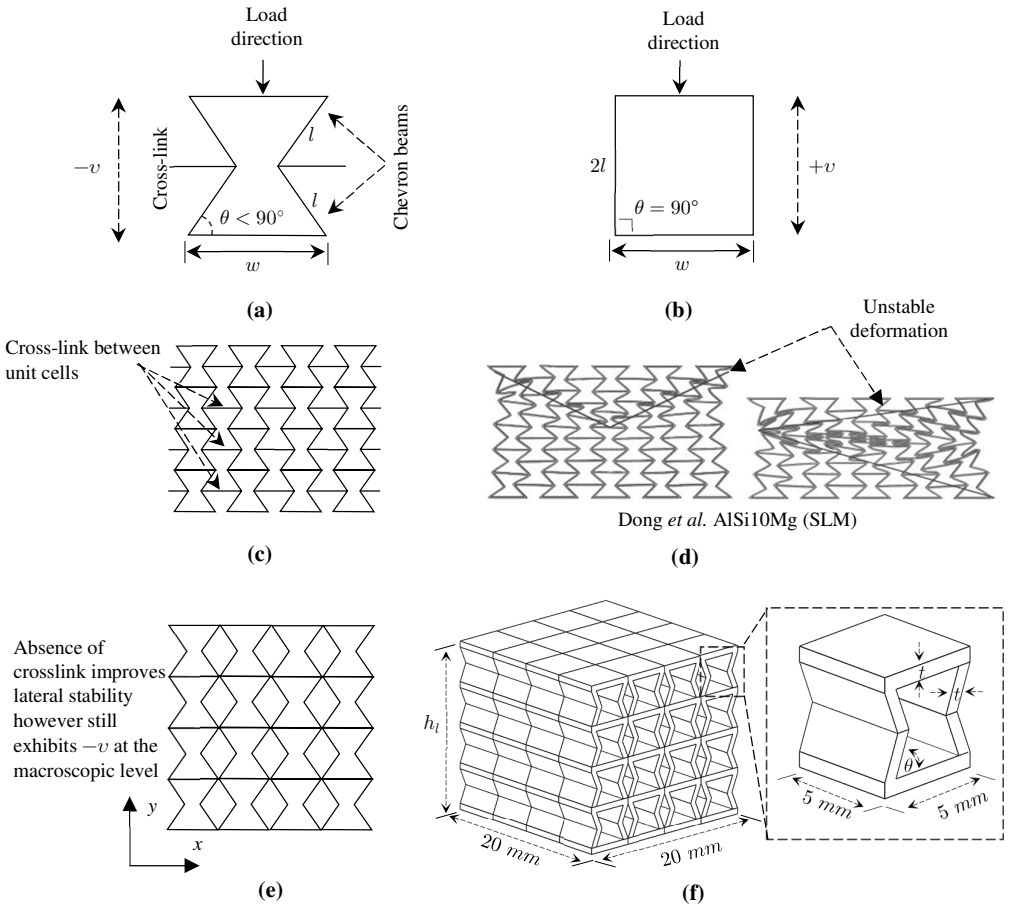

Fig. 1. Design evolution of the laterally stable $-\boldsymbol{\upsilon}$ structure showing **(a)** traditional re-entrant unit-cell, **(b)** the non-auxetic variant when the angle is at or above 90°, **(c)** traditional assembly of the auxetic unit cell featuring crosslinks **(d)** unstable response of the traditional architecture observed by Dong *et al.* [126] when replacing beams with thin and thick walls (0.3-1 mm), **(e)** Re-entrant assembly without crosslink allowing for lateral stability through continuous layer formation and **(f)** the geometric configuration of the 3D $-\boldsymbol{\upsilon}$ structure considered in this study where $\boldsymbol{t}$ and $\boldsymbol{\theta}$ are the design variables.

Beam based models of the traditional bowtie architecture have been extensively studied over the past years [127–130]. On the contrary performance of surface/sheet/plate-based variant of this architecture are yet to be studied. Dong *et al.* [126] conducted a brief study mimicking the traditional architecture as shown in Fig. 1c using thin (0.3 mm) and thick (1 mm) walls.

However, the resulting deformation of the wall variant of the traditional auxetic architecture shows an inherently unstable behaviour (Fig. 1d). The reason for this is the prevalence of dominated localised buckling due to limited lateral support. With a view to identifying alternatives, this study conceives a new arrangement inspired from the traditional re-entrant unit-cells without the use of crosslinks as shown in Fig. 1e. The design approach leads to a layered architecture that is inherently stable. The term layered is used to characterise the continuous lateral wall formed as a result of the unit-cell arrangement represented by straight horizontal lines in Fig. 1e. This can ultimately lead to the development of functional and stable thin-thick walled negative Poisson's ratio structures that can be additively manufactured.

Based on the layer-based design philosophy, the structure is conceived as shown in Fig. 1f. Thin and thick-walled variants are then created by simply modulating the thickness t between 0.3 and 1 mm. The other design parameter is the angle (θ); when θ is 90° the behaviour of the unit-cell yields a positive Poisson's ratio, consequently θ ranged between 45° and 85° to preserve $-\upsilon$. To ensure a parametric comparison the global length in x and z are kept constant at 5 mm, the y distance (hereafter referred to as height h) is dictated by θ as the length (l) of chevron beams are kept constant in all design variants. Consequently, h was not intentionally designed but determined after the other parameters had been fixed. In this aspect, the relative density of the unit cell ($_{uc}$) is the ratio of volume of unit-cell to the apparent volume of the unit cell which is a cuboid of $5 \times 5 \times h$ (mm).

The global architecture was then conceived by linear patterning the unit cell in x, y and z direction. The resulting design has a global dimension of 20×20 mm across the width (x) and breadth (z) as shown in Fig. 1f. However, the height (h_l) varied according to the angle resulting in a maximum height of 20 mm when the angle (θ) was 90° at a 1 mm thickness (t). A minimum height of 13.32 mm resulted at a 45° angle and 0.3 mm thickness. A total of nine different designs were conceived dictated by the DoE algorithm which represented a combination of t and θ. The parametric model was advised by the central composite design (CCD) DoE model which is discussed in subsequent sections.

2.2. Design of experiments

2.2.1. Response surface model

Response surface (RS) models were generated to fully understand the influence of geometrical parameters and their interaction on the mechanical performance of the structures. RS models consist of a group of mathematical and statistical techniques that are based on the fit of empirical models to the experimental data. This is done by employing polynomial functions to describe the behaviour of the structure and to explore their parametric influence. Consequently, this study employs the response surface methodology for the design of experiments (DoE) in parallel with physical experimental testing.

Numerous variables can affect the behaviour of the structure being studied; however, it is unfeasible to identify and control contributions from each one. Therefore, it was necessary to select those variables that allow for major effects on the auxetic behaviour, which in this case is the wall thickness (t) and angle (θ). Accordingly, the model considered in this study is represented using five responses namely the elastic modulus (E), compressive strength (σ_c), failure strain (ε_f), Poisson's ratio (υ) and relative density ( ). By fitting the experimental data to suitable polynomial equations, the RS model can provide a prediction that can be used to indicate which design parameter has the most influence on the mechanical performance of the structure. Furthermore, the RS models can be also extended to study the interaction effects between the geometrical parameters for each of the responses considered. The key steps used in the construction of the RS model is summarised in Fig. 2.

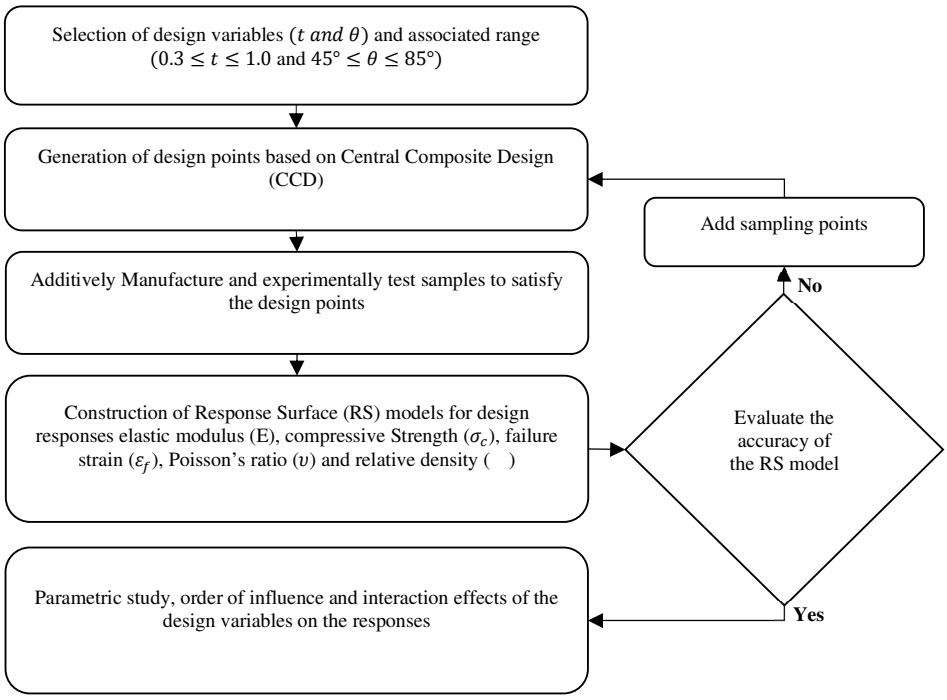

Fig. 2. DoE process used to obtain the Response Surface (RS) model used for the parametric analysis.

2.2.2. Sampling design points

The RS model was developed using a Central Composite Design (CCD) where the independent design variables and the parametric range is summarised in Table 1. The thickness (t) ranged between minima and maxima of 0.3 and 1 mm. The selected thickness range provides a good balance between the quality of the generated structure and its capability to deform sufficiently under loading. Angle (θ) ranged between minima and maxima of 45° and 85°. Any further reduction in θ ($< 45°$) will cause the chevron beams interacting with the sides of the unit cell resulting in incomparable behaviour. The upper limit of 85° was the smallest angle that resulted

in traditional lattice behaviour as shown in Fig. 1b. Accordingly, the upper limit was chosen to preserve the re-entrant behaviour of the cellular structure studied.

Table 1. Variables and experimental design levels used for the CCD RS model.

Variable	Code	-1	0	1
t (mm)	A	0.3	0.65	1.0
θ (deg)	B	45	65	85

The selection of the geometrical variables and experimental design were based on the CCD RS model to cover the typical range to enable the re-entrant behaviour. While Poisson's ratio (υ) is the parameter representing the re-entrant behaviour, the elastic modulus (E), compressive strength (σ_c) and failure strain (ε_f) quantify the mechanical performance at the elastic and plastic behaviour of the structures. Lastly the relative density ( ) allows to quantify the amount of material being used by the model. Based on the design matrix, prototypes were manufactured using SLM and physical experimental tests carried out for all the sampling design points.

2.3. Material and manufacture

A total of 27 sample prototypes satisfying design sampling points were additively manufactured using AlSi10Mg alloy having a material composition listed in Table 2. A Powder Bed Fusion (PBF) machine featuring a 400 W fibre laser was used. The laser sintering of the material was conducted through an overhead laser system that modulates based on the process parameters such as laser exposure of 370 W, scan speed of 1300 mm/s, layer thickness of 30 µm and a 190 µm hatch distance. These parameters were selected as they were found to be optimum for the size of the smallest wall thickness (0.3 mm) being manufactured and resulted in a 99.8% dense part. After the first layer of powder has been processed, the build platform was lowered by one increment and another layer of powder is deposited on to the bed using a re-coater at a dosing factor of 140%. The laser then melts the new layer of material fusing it with the previous layer and the process repeats.

Table 2. Material composition (*wt.* %).

Al	Si	Fe	Cu	Mn	Mg	Ni	Zn	Pb	Sn	Ti
Bal.	9.0	0.55	0.05	0.2-0.45	0.25-0.45	0.05	0.10	0.05	0.05	0.15

The AlSi10Mg powder used for the production run was gas atomised to obtain a nearly spherical shape sieved for a particle size of >90 µm. The laser melting was carried out using the contour-hatch strategy, where the 2D layer data from the CAD geometry was used to offset the melt-pool width for high geometrical accuracy. The contours were then traced by the laser followed by the hatch scans to fill the enclosed area. The contour scan diameter was set to match with the laser spot size to ensure further interpolative calculations were not necessary. This technique was found to deliver the most repeatable AlSi10Mg parts irrespective of the struct thickness variation dictated by the DoE matrix ($0.3 \leq t \leq 1$ mm).

Table 3. Bulk properties of SLM AlSi10Mg.

Mat.	ρ (kg/m^3)	ρ_r(%)	E (GPa)	σ_y (MPa)	σ_t (MPa)	ε_f	υ
AlSi10Mg	2670	99.85	70	230	345	0.03	0.3

SLM was conducted in an environment initially vacuumed and then backfilled with 99.995% pure Argon with an Oxygen content of ~0.1%. The build platform was heated to 80 °C before the melting began and the whole process took approximately 9 hrs to build. Internal support structures were not possible with the lattices due to the challenges associated with removing them. To overcome this, a self-supporting diagonal build technique with external supports was adopted. The printed prototypes were heat-treated at 300 °C for 2 hrs. Following heat treatment, the specimens were removed from the build plate support using submerged wire Electro-Discharge Machining (EDM). The bulk material properties of AlSi10Mg additively manufactured using SLM under identical conditions are listed in Table 3, where , , E, σ_y, σ_t ε_f and υ are the density, relative density, Young's modulus, yield strength, tensile strength, failure strain and Poisson's ratio respectively.

2.4. Experimental testing

Compression tests were performed using a Zwick Roell Z1474 universal materials test rig (Fig. 2a) having a maximum load capacity of 100 kN. The tests were carried out to obtain the stress-strain ($\sigma - \varepsilon$) responses for all the design sample points. Before commencing the tests the rig was calibrated and verified following BSENISO 7500-1 [131]. All test samples were loaded to a maximum deformation of 30% of the original height through crosshead displacement at a rate of 0.01 mm/s.

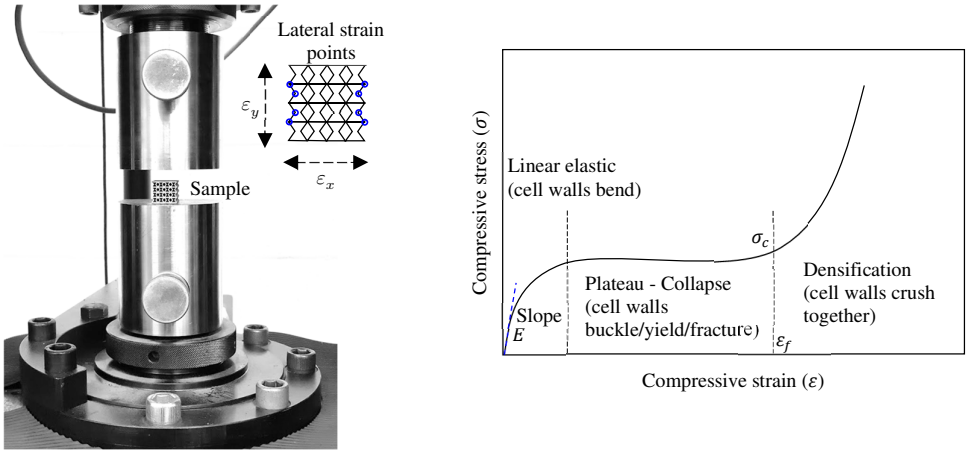

(a) **(b)**

Fig. 3. Experimental test of the porous structure showing (a) the test rig and (b) a representative example of the corresponding responses.

A deformation-controlled load was applied to prevent the test from stalling at the elastic limit. Nevertheless, a maximum load of 80 kN with a force shutdown threshold of 50% was used to prevent the platens from colliding in the event of a catastrophic failure. Deformation beyond the

elastic limit was essential to study the failure modes and the overall behaviour of the auxetic structures. Real-time force-displacement ($f-\delta$) and $\sigma-\varepsilon$ curves were obtained using an effective contact area of 400 mm^2. Based on the $\sigma-\varepsilon$ curve, the properties of the test samples were characterised for E, σ_c, ε_f as defined in Fig. 3b. While E represented the linear slope in the elastic region, the compressive strength (σ_c) and failure strain (ε_f) is measured as the peak stress and corresponding strain at the plateau region just before the onset of the densification regime.

Precise measurement of Poisson's ratio (υ) is still a challenging problem for geometrically porous materials. The accuracy of υ to a large extend depends on the methodology used for measuring the lateral strain. In this study, the axial (ε_y) and lateral strain (ε_x) to calculate υ was measured using the crosshead movement and fine strain extensometer (Zwick) respectively. The transverse elastic strain was measured by monitoring the displacement of eight boundary points as shown in Fig. 3a and the average strain was used to compute υ, a method similar to Xue *et al.* [132]. Based on the experimentally measure average strain data, Eqn. (1) was used to calculate the Poisson's ratio.

$$\upsilon_{yx} = -\frac{\langle \varepsilon_x \rangle}{\langle \varepsilon_y \rangle} \tag{1}$$

3. Results and discussion

3.1. Geometrical variation of SLM prototypes

The as build SLM AlSi10Mg prototypes based on the geometrical parameters dictated by the DoE matrix are shown in Fig. 4. Upon completion of the build, the parts were removed from the build plate using Electrical discharge machining (EDM). As expected with DMLS, a rough surface finish was created due to the layer-by-layer process SLM process. Even though Bai *et al.* [133] demonstrated a 99.9% density for SLM AlSi10Mg parts under the optimum process, a few studies [134–136] demonstrated density variation depending upon the material thickness of the part. Since density variation can directly affect the mechanical performance and the strain to failure, the relative density ( ) of the AlSi10Mg were analysed and compared to quantify any variation.

One of the most economical ways to get information about the quality of laser melted part is the measurement of [137]. Accordingly, Fig. 5 compares the relative density of the SLM prototypes with ideal values calculated from the respective CAD geometry. Analysing the influence of the angle on (Fig. 5a), a highest difference of 4.86% was observed at 67.5°. When the angle increased to 85°, the difference reduced to 0.88%. The trend was similar when the angle was lowered (<67.5°) and exhibited a difference of 1.70% at 45°. This shows that the SLM process resulted in a 1.88-4.86% geometrical variation with the worst case at 67.5°. However, in comparison to the observations reported by Weißmann *et al.* [138] at 9-14% on Ti6Al4V

depending on the strut angle, the performance here is significantly smaller and well within acceptable limits.

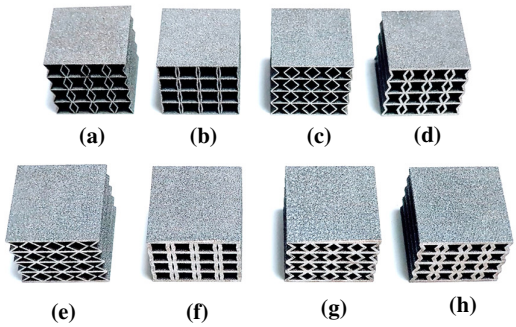

Fig. 4. SLM AlSi10Mg prototypes for experimental testing were **(a)** t=0.30 mm, $\boldsymbol{\theta}$=67.50° and $\boldsymbol{\rho_r}$= 0.20, **(b)** t=0.40 mm, $\boldsymbol{\theta}$=85° and $\boldsymbol{\rho_r}$= 0.27, **(c)** t=0.40 mm, $\boldsymbol{\theta}$=51.59° and $\boldsymbol{\rho_r}$= 0.29, **(d)** t=0.65 mm, $\boldsymbol{\theta}$=67.50° and $\boldsymbol{\rho_r}$= 0.40, **(e)** t=0.65 mm, $\boldsymbol{\theta}$=45.00° and $\boldsymbol{\rho_r}$= 0.47, **(f)** t=0.90 mm, $\boldsymbol{\theta}$=85° and $\boldsymbol{\rho_r}$= 0.50, **(g)** t=0.90 mm, $\boldsymbol{\theta}$=51.59° and $\boldsymbol{\rho_r}$= 0.52 and **(h)** t=1.00 mm, $\boldsymbol{\theta}$=67.50° and $\boldsymbol{\rho_r}$= 0.56.

Studying the effect of wall thickness on the measured relative density as shown in Fig. 5b, the highest difference of 9.85% was observed between the ideal geometry and the SLM prototype at the lowest thickness of 0.3 mm. However, as the thickness of the part increased to 0.65 mm and 1 mm, the difference in decreased to 4.86% and 1.12% respectively. Even though the overall discrepancy is below 9.85%, it can be seen that t has a higher influence in comparison to θ on the quality of the AlSi10Mg SLM parts.

Studying the thin-walled structure (0.3 mm) under the scanning electron microscope (SEM) as shown in Fig. 6 reveals the influence of surface roughness on the overall thickness of the wall. It can be seen that the thickness of both inclined (Fig. 8a) and horizontal walls (Fig. 8b) have been significantly affected by the infringement of the surface roughness and partially fused particles; a salient feature of the SLM process.

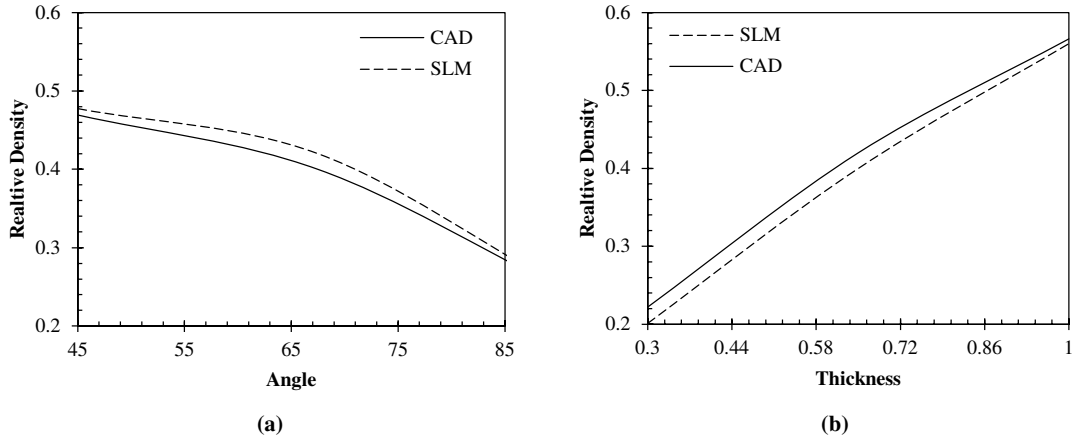

Fig. 5. The influence of SLM process on the relative density of AlSi10Mg prototypes in comparison to the ideal CAD geometry where **(a)** shows the effect of auxetic angle and **(b)** the thickness.

The observation can be related to Maamoun *et al.* [139] where a dimensional tolerance of 0.15 and 0.195 mm was observed for laser melted AlSi10Mg parts featuring thicknesses at or below 0.3 mm. This explains the reason for the higher significance of t on the variation in relative density in comparison to θ. While the effect of angle is limited to the inclined walls alone, the thickness has an effect on all walls and hence the higher significance. The double the number of overall walls, as opposed to inclined walls, explains why the discrepancy in is almost twice for t (9.85%) in comparison to θ (4.86%).

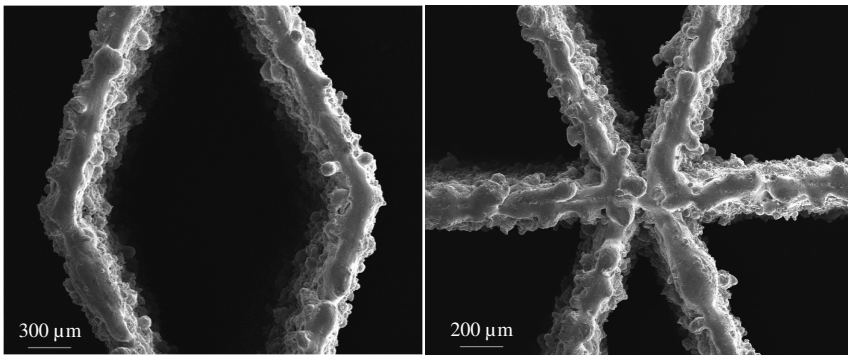

Fig. 6. SEM analysis of the AlSi10Mg structures at a wall thickness of 0.3 mm showing **(a)** the influence of surface roughness on the overall thickness of inclined thin walls and **(b)** the quality of junction along with horizontal walls.

3.2. Design parameters and mechanical performance

To better understand the mechanical behaviour of the layer-based re-entrant architecture, the influence of the individual geometrical parameters are studied. This was found to be critical in understanding the interaction effects of the thickness and angle on the compressive behaviour using the response surface model. Therefore, a systematic understanding of the individual parameters are sought. Fig. 7 shows that the structures exhibit a similar initial compressive behaviour comparable to a typical porous solid. However, the transition from elastic to plastic region is gradual and progressive resulting in a smoother curve in comparison to cellular solids. This means that the failure is initiated as a buckling event similar to traditional auxetic materials which then progresses on to take continuous load before ultimate failure. Similar to porous materials, the $\sigma - \varepsilon$ progression is followed by an apparent yield point (σ_y) and a compaction region with a constant stress plateau followed by a region of localised densification.

The densification region is due to the compaction of the plastically failed material and starts earlier in auxetic structures in comparison to general porous structures. This is due to the inward compaction of the material owing to the negative Poisson's ratio. Furthermore, the $\sigma - \varepsilon$ behaviour of the structures exhibited a relatively short but high plateau region resulting in compressive strength at higher strains in comparison to porous or traditional cellular materials of comparable relative density. This enhanced effect can be attributed to the geometry of

structure that not only results in a negative Poisson's ratio but also higher failure strain (ε_f) as a result of the complex stress distribution and deformation of the walls supported by the stable layers.

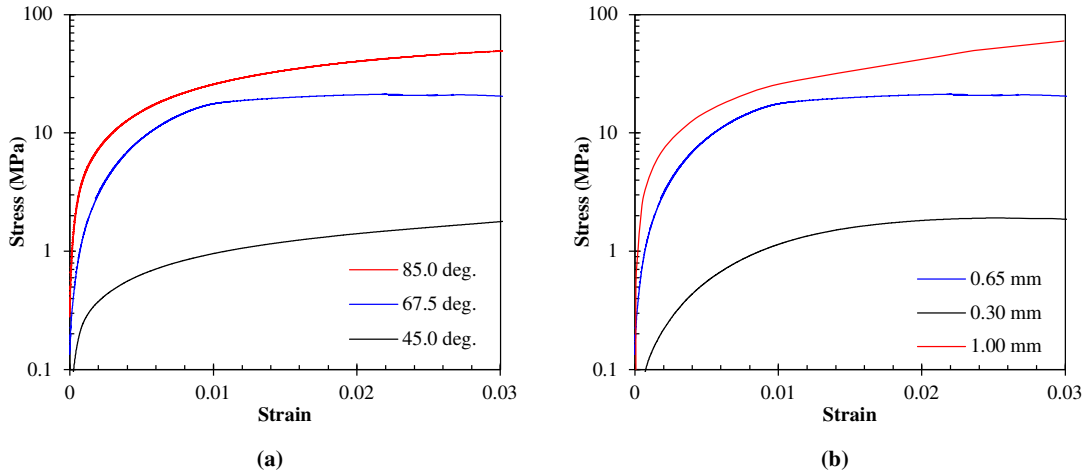

Fig. 7. Stress-strain performance of the SLM prototypes showing **(a)** the influence of angle at a thickness of 0.65 mm and **(b)** the influence of wall thickness at 67.5°.

Looking at the effect of the angle (Fig. 7a) and wall thickness (Fig. 7b) on the $\sigma - \varepsilon$ behaviour, a significant effect on the mechanical performance under both cases were observed. Even though the overall $\sigma - \varepsilon$ profile was representative of buckling induced failure, the characteristic performance was highly dependent on the design parameters t and θ. It is clear that increasing θ increases both the quasi-static stiffness represented by the elastic modulus (E) and compressive strength (σ_c). The trend was found to be similar when t increased at a constant angle.

Extracting the characteristic mechanical responses as shown in Fig. 8, it is clear that both the design variables θ and t have a significant influence on the elastic modulus (E), compressive strength (σ_c), failure strain (ε_f) and Poisson's ratio (υ). Keeping a constant thickness of 0.65 mm and varying θ from 45° to 85°, the elastic modulus of the structure increased almost linearly from 0.115 to 1.795 GPa (Fig. 8a); a 175% improvement in the elastic modulus. Even though a similar overall trend can be observed in Fig. 8b, increasing the thickness from 0.3 to 1 mm increased E from 0.063 to 1.644 GPa, which is an increase of 185%.

The relationship between θ and E of the lattice structure observed can be related to works of Whitty *et al.* [140], who also found that increasing the angle while keeping constant thickness leads to an improvement in elastic modulus for auxetic beam models. This shows that when it comes to stiffness the wall-based $-\upsilon$ structure despite featuring a modified re-entrant architecture perform similar to beam-based architecture of comparable thickness. This influence of θ on E of the structure can be potentially used to optimise the stiffness of structures to achieve target values at any given porosity. This can have a significant effect on the development of

stiffness matched implants and bone scaffold with targeted performance to reduce stress shielding and maladapted stress concentration [141–146].

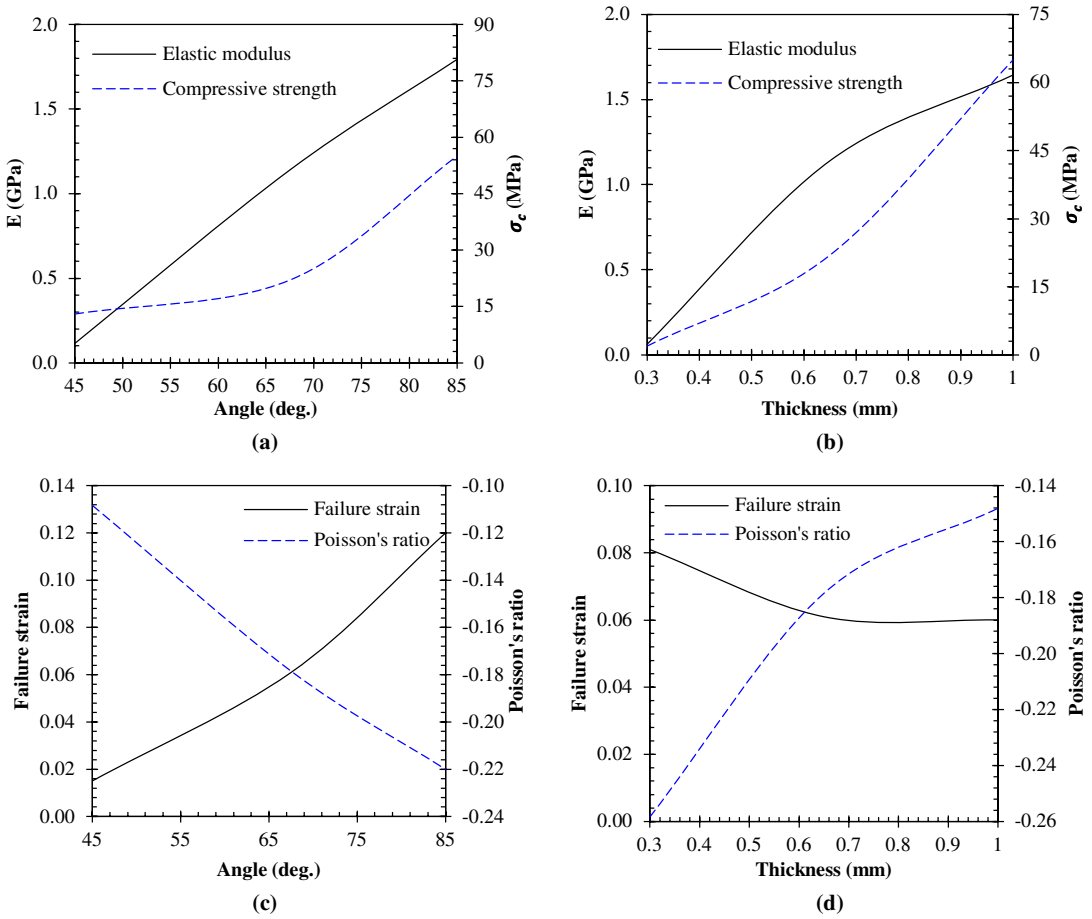

Fig. 8. Influence of design parameters on the mechanical performance of the structure showing **(a)** influence of angle on the elastic modulus and compressive strength at a thickness of 0.65 mm, **(b)** influence of thickness on the elastic modulus and compressive strength at an angle of 65°, **(c)** influence of angle on the failure strain and Poisson's ratio at a thickness of 0.65 mm and **(d)** influence of thickness on the failure strain and Poisson's ratio at an angle of 65°.

The increase in E with respect to t can be validated by relating the thickness to the relative density of the overall structure. It can be seen from Fig. 5b that increasing t affects thus reducing the porosity and increasing the stiffness. Nevertheless, the two distinct slopes in the rise up to the maximum E while increasing t is partly due to the influence of surface roughness on the performance at a lower thickness (0.3 to 0.6 mm) as shown in Fig. 6. This means that when t increases from 0.3 to 0.6 the rate of increase in E is higher in comparison to the later part (0.6 to 1 mm). Furthermore, the rate of increase in E towards the later part of the slope (0.6 to 1 mm) can be seen to be gradually decreasing. Overall increasing either θ or t increases the stiffness of the structure with the influence of t reducing as the relative density tends to unity.

An increasing trend was also observed for σ_c as shown in Fig. 8a and 8b where the thickness seems to have a higher influence in comparison θ. When θ increased from 45° to 85°, σ_c increased

from 13 to 55 MPa (~124%). However, within this range, the increase from angle 45° to 65° was gradual at 13 to 22 MPa (~51%) in comparison to the later part (65°-85°) where the rise was almost two folds. On the other hand, when t increased from 0.3 to 1 mm, the rise in σ_c was almost linear from 1.95 to 65 MPa (~188%). While it is clear that t take precedence when it comes to achieving the highest compressive strength. This can be primarily attributed to the buckling induced failure phenomenon of the auxetic structured considered.

It is apparent that increasing either thickness or angle will inevitably lead to higher stiffness (E) and strength (σ_c) of the layer-based re-entrant architecture under investigation. The observation is comparable to that of Al traditional re-entrant beam-based auxetic structures manufactured using investment casting by Xue *et al.* [132]. This goes to show that removing the crosslinks and having continuous layers not only adds lateral stability but returns comparable behaviour to traditional re-entrant arrangement. However, it is important to remember that a higher t leading to increased E and σ_c is not reserved for auxetic structures, increasing thickness in any lattice structure will lead to an increase in relative density while decreasing porosity hence leading to higher stiffness and strength characteristics. Therefore, the difference when it comes to auxetic structures is that of θ dictating improvements in E and σ_c. For example, a 20% increase in angle resulted in 36% and 60% increase in elastic modulus and compressive strength respectively.

In an attempt to quantify the influence of strain in improvement σ_c as a result of the design parameters, the failure strain (ε_f) is analysed with respect to θ and t as shown in Fig. 8c-d. Significant improvement in σ_c with respect to increasing angle was found to be the result of increasing elastic strain as shown in Fig. 8c. As θ increasing, the structure seems to be accommodating a larger elastic strain before the start of plastic failure. Overall, an almost linear increase in ε_f was observed as the angle increased from 45° to 85° reaching the highest strain of approximately 12%. This means that at larger angles the structure is effective at distributing the load within all layers of the structure allowing strain rates far superior to regular lattice or cellular structures.

Looking at the influence of t as shown in Fig. 8d, ε_f was found to decrease gradually from 8% to 6% as the thickness increased from 0.3 to 0.6 mm. On the subsequent rise in t, the strain rate remained more or less constant within a ±1% variation. Therefore, the initial decrease in ε_f for thin-walled specimens (0.3-0.6 mm) can be attributed to the influence of SLM process leading to geometrical irregularities demonstrated in Fig. 6. With the increase in thickness the influence of the process parameter on ε_f decreased eventually leading to a constant strain of 6%. Accordingly, the failure strain at higher thicknesses (>0.6 mm) can be attributed to the intrinsic property of the material rather than the geometrical architecture.

It is well known that conventional materials experiencing a compressive load expand along the lateral direction, the resulting negative ratio of transverse to longitudinal strain defines the Poisson's ratio (υ). Due to its association with the overall rate of deformation of the cross-section

of a structure, υ is considered a substantial mechanical response, as it can dictate to a certain extent the structural stability at the macroscopic level [147–150]. As opposed to conventional materials a particular feature of the re-entrant architecture is the negative Poisson's ratio [151–153]. Fig. 8c and 8d show that all the variation of the thin and thick-walled structures despite the absence of the traditional crosslink exhibits negative Poisson's ratio ($-\upsilon$). An overall variation between -0.11 and -0.26 was observed between the limits of the geometric variables introduced. A range comparable to Al auxetic structures that feature a conventional beam based re-entrant architecture [126,132,154]. However, it is important to recognise that the structures exhibit average $-\upsilon$ despite allowing both lateral expansion and compression. Even though the layer-based architectures allow for a small lateral expansion along the straight plates connecting each row, the overall behaviour is still dominated by the lateral compression of the chevron layers resulting in $-\upsilon$.

Evaluating the influence of θ on υ as shown in Fig. 8c, the space within the layers increases with the rise in θ while reducing (Fig. 5a). Increasing θ results in increased porosity of the structure which, in turn, accommodate a higher lateral strain increasing the absolute value of υ as θ increases. On the contrary, increasing t decreases the absolute value of Poisson's ratio as shown in Fig. 8d. When t increased from 0.3 to 0.7 mm the decrease in the absolute value of υ was almost linear from -0.26 to -0.18 (~30%). Though the trajectory of υ continues to decrease as t rises from 0.7 to 1 mm, the rate of decrease was lower at -0.18 to -0.15 (~20%). This is due to the increased interaction between chevron beams due to the thicker walls. It is also important to take into consideration that thick walls not only decrease porosity but also reduces the length of the chevron beams. This suggests that increasing t has a similar effect on decreasing l on υ. Furthermore, higher t enhances the structural rigidity and resistance to deformation also contributing to a reduction in the absolute value of the Poisson's ratio.

3.3. Failure mode analysis

In order to study the effect of the design parameters on the failure of the layered structure, the samples post-compression were examined. Despite featuring a range of design parameters, the resulting deformation mode and associated failure can be categorised into either of the two cases shown in Fig. 9. The behaviour of both thin ($0.3 \leq t < 0.65$ mm) and thick ($0.65 < t \leq 1$ mm) walled samples showed stable and progressive deformation and failure as shown in Fig. 9a and 9b respectively; a significant improvement in comparison to the thin and thick-walled traditional auxetic architecture reported by Dong *et al.* [126]. The reason for the stable deformation can be attributed to the enhanced lateral support offered by the sandwich walls limiting unstable buckling global. Although numerous studies [44,155–157] exist on the mechanical behaviour of AM metallic $-\upsilon$ structures, these are to a large extent limited to beam-based models. On the contrary, systematic studies of the failure mechanisms of $-\upsilon$ walled/surface/plate/sheet-based AM structures are rare; an observation also reported in a comprehensive review by Zadpoor [72]

on biomedical application. However, additively manufactured honeycomb structures exhibiting $+v$ under the influence of in-plane compression have been extensively studied [158–163].

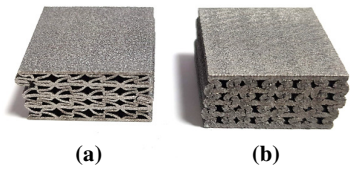

Fig. 9. Uniformly compressed SLM samples showing **(a)** thin-walled structure showing progressive folding at $\boldsymbol{\theta}$=45° and (b) thick walled structure showing stable folding at $\boldsymbol{\theta}$=65°.

To further study the failure behaviour at both the micro and macro-scales, the failed samples were investigated under an SEM as shown in Fig. 10. For non-auxetic cellular structures of similar thickness and overall dimension, the weak spots created by the SLM process is often cited to drive the failure process [117,164,165]. The reason for this is the localised stress concentrations that appears at the weak spots facilitated by SLM as shown in Fig. 6 long before the material yields; an observation similar to Yu *et al.* [166] while studying beam based AlSi10Mg micro-lattices. The process-induced weak spots allow strain intensification on continued loading ultimately leading to fracture and overall failure.

In comparison, Fig. 10 shows that the failure of the layered re-entrant structure presented is primarily prescribed by the geometry and the associated wall thickness as opposed to SLM induced discrepancies. This is because the failure is associated with buckling of the chevron walls which is dictated by the geometry. The deformation at lower angles ($\leq$67.7°) presented in Fig. 10a is a result of the progressive folding of the chevron walls where the horizontal walls can be seen to bend to accommodate the shrinkage driven by the folding chevron walls. From the resulting deformed unit-cell shown in Fig. 10b, it is clear that the fractured surface resembles a buckling induced bending failure. Extension and thinning of the chevron walls are also visible from Fig. 10a and 10b evidencing a combination of semi-ductile and brittle behaviour, which is often observed for SLM AlSi10Mg [117,167,168]. Furthermore, the failure is dependent on the collapse of individual unit-cells subsequently leading to layers; a distinction in comparison to traditional cellular structures where a shear planes through the entire structure is often observed [169–171].

At higher wall thicknesses the wall deformation was short-lived in comparison to their thinner counterparts without any macroscopically localised phenomenon as shown in Fig. 10c and 10d. On the progression of the compressive strain, the thick chevron walls deformed and interfered with the lateral walls subsequently leading to overall failure as shown in Fig. 10c. Extracting the behaviour of a single unit-cell, cracks can be observed at both ends of the chevron walls as opposed to a single section observed in thin-walled samples. A further distinction was observed regarding the deformation of the horizontal walls. Rather than bending as observed for thin walls wrinkling of the horizontal beams can be seen to accommodate the global negative strain visible

through the dimpled horizontal walls as shown in Fig. 10d. In this regard, the failure resembles the macroscopic case of auxetic cellular tubes studied by Karnessis and Burriesci [172]. Accordingly, it can be summarised that the failure of the layered re-entrant structures is due to the deformation of chevron walls dominated by the unit-cell shape, which can be classified as buckling induced bending failure.

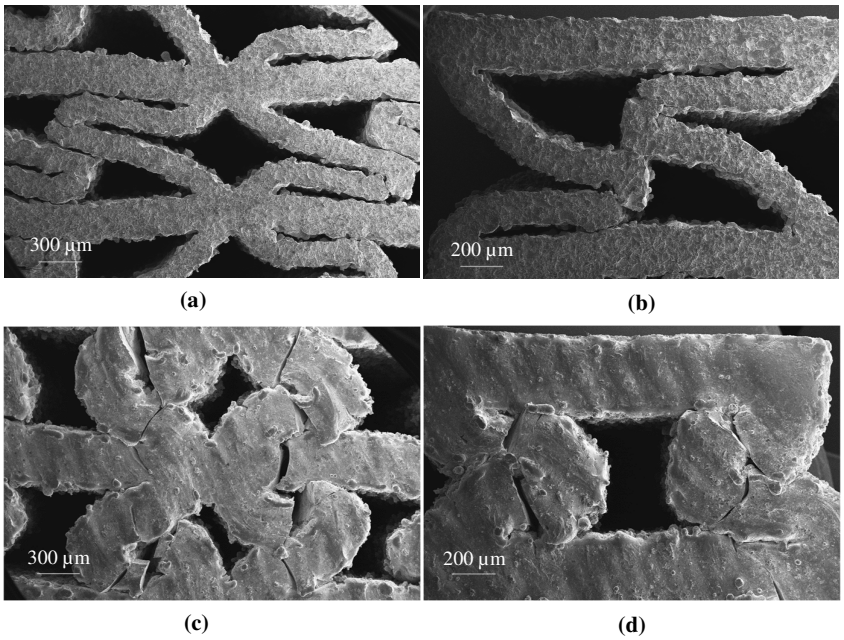

Fig. 10. Fracture surface of the failed samples observed under SEM showing **(a)** progressive folding of thin-walled samples (<0.65 mm), **(b)** crack propagation and folding pattern for a thin-walled unit-cell, **(c)** collapse behaviour of thick-walled (1 mm) sample and **(d)** failed thick-walled unit-cell.

3.4. Parametric interaction analysis

3.4.1. Response surface model

After having established the influence of the individual parameters on the mechanical response through classical analysis; the important question to ask is 'what favourable combinations of the design parameters offer the desired response?' Since the study is not targeting a particular response, the question has to be answered in more generic terms. In order to answer this question, the RS model is used to study both the interaction effects and order of influence of the design variables on the mechanical performance. The analysis so far on the independent effects of the design parameters aided in understanding their contribution to the overall mechanical performance. However, the interaction effects between the geometrical parameters of the structure, *i.e.* t and θ, along with how such interaction may influence the mechanical performance and relative density of layered re-entrant structure is still not clear. This is also an area of deficiency when it comes to the available literature on auxetic structures in general. An aspect tackled in this study through the generation of response surface (RS) models.

The approach used the stepwise regression methodology that represents the experimental data through relevant polynomial equations. The equations were then extrapolated to identify relevant model terms based on how well the equation fits the experimental data. The stepwise regression was chosen as it eliminates the insignificant model terms automatically from the polynomial equation [173,174]. The statistical significance of the models and each term in the regression equation were evaluated using statistical measures that achieve the best fit [175].

Table 4. The DoE matrix based on Central Composite response surface model.

Factor 1	**Factor 2**	**Responses**				
A = t (mm)	B= θ (deg.)	E (GPa)	σ_c (MPa)	ε_f	υ	
0.65	65	1.14	22.10	0.061	-0.178	0.40
0.65	65	1.14	22.10	0.061	-0.178	0.40
0.65	65	1.14	22.10	0.061	-0.178	0.40
0.40	85	0.90	13.13	0.019	-0.257	0.27
0.30	65	0.06	01.95	0.081	-0.220	0.20
0.65	45	0.12	13.13	0.015	-0.108	0.47
0.65	65	1.14	22.10	0.061	-0.178	0.40
0.89	52	0.70	30.21	0.002	-0.128	0.52
0.40	52	0.04	00.25	0.140	-0.154	0.29
1.00	65	1.64	65.10	0.049	-0.150	0.56
0.89	85	1.79	60.11	0.120	-0.156	0.50
0.65	65	1.14	22.10	0.061	-0.220	0.40

SLM prototypes were generated to satisfy the design variables associated with sampling design points. Experimental measurements were carried out on the samples and the responses of interest (E, σ_c, ε_f, υ and) were determined as listed in Table 4. The best-fit indicators on the experimentally measured responses show that E, σ_c and can be characterised by linear models listed in Eqn. (2), (3) and (6) respectively. On the other hand, the υ and ε_f requires quadratic models in Eqn. (4) and (5) to adequately navigate the design space.

$$E = -2.40994 + 1.90273t + 0.031661\theta \tag{2}$$

$$\sqrt{\sigma_c} = -6.08103 + 9.31808t + 0.068466\theta \tag{3}$$

$$\sqrt{\varepsilon_f} = 1.04522 - 2.449t - 0.000522\theta + 0.032137t\theta + 0.123865t^2 - 0.000139\theta^2 \tag{4}$$

$$\upsilon = 0.339190 - 0.199667t - 0.012616\theta + 0.004528t\theta + 0.004143t^2 + 0.000056\theta^2 \tag{5}$$

$$= 0.177124 + 0.486869t - 0.001408\theta \tag{6}$$

The analysis of variance (ANOVA) was used to model the significance of each of the geometrical parameters on the resulting mechanical performance. Accordingly, Table 5 summarises the significant model terms and the adequacy measures as a result of ANOVA. The adequacy measures of the model are the probability (p-value), coefficient of determination R^2, Adjusted R^2, Predicted R^2, and Adequate precision.

Table 5. Analysis of variance for the response surface models generated.

Model	F-value	p-value	Statistical measurements			
			R^2	$Adj\text{-}R^2$	$Pre\text{-}R^2$	*Adeq-precision*
E	43.81	<0.001	0.9069	0.8862	0.8182	20.4288
σ_c	198.39	<0.0001	0.9778	0.9729	0.9467	38.9586
ε_f	80.77	<0.0001	0.9854	0.9732	0.8150	29.5262
υ	14.32	0.0028	0.9227	0.8583	0.8027	12.9798
	159.52	<0.0001	0.9726	0.9665	0.9336	35.0741

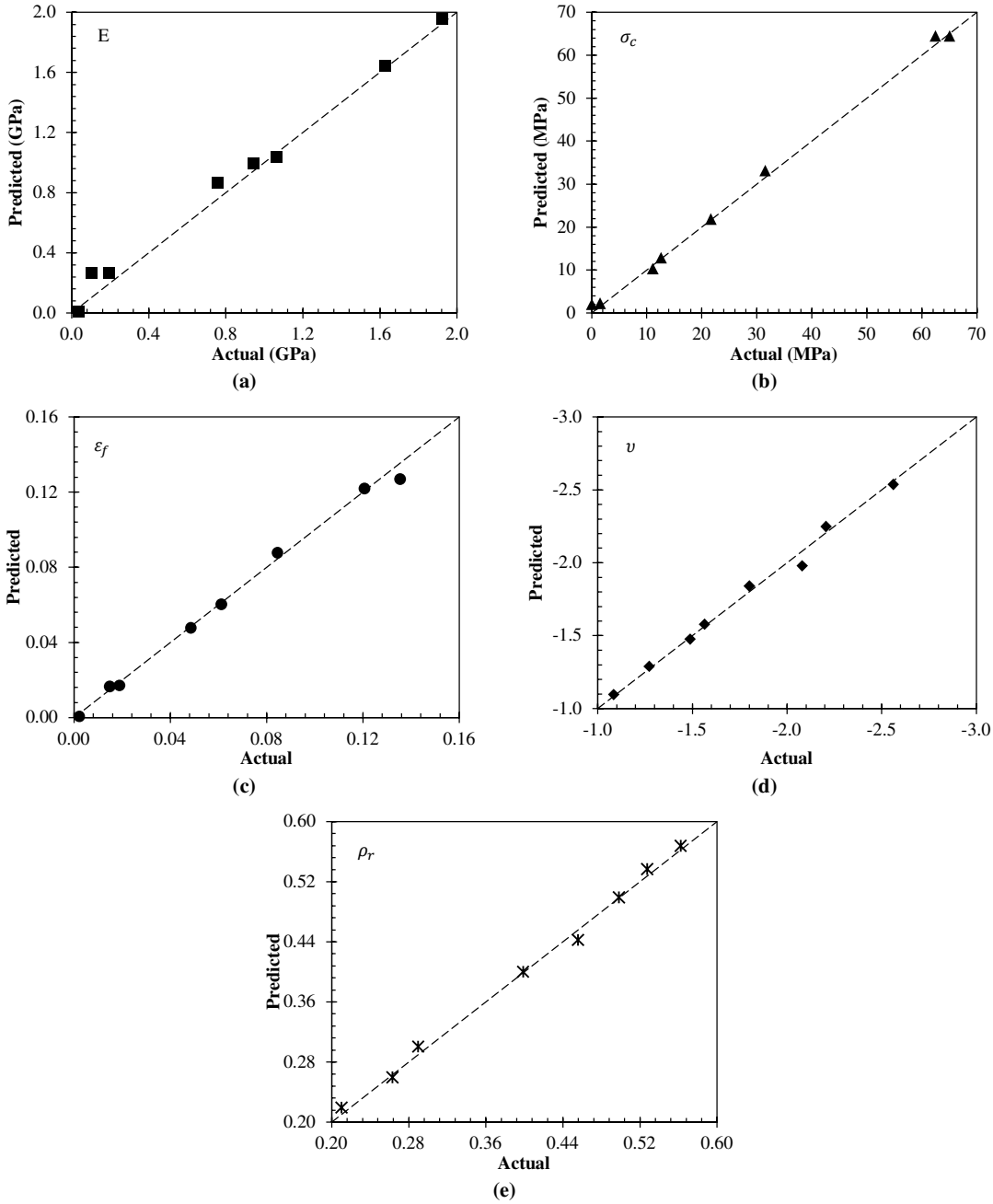

Fig. 11. Comparison between experimental and predicted results using the response surface model generated for **(a)** elastic modulus, **(b)** compressive strength, **(c)** failure strain, **(d)** Poisson's ratio and **(e)** relative density.

From Table 5, it is clear that all models feature high F-values and very low p-values, which validates that all the four models are statistically significant [176]. P-values less than 0.05 indicate that model terms are significant [177]. Additionally, a higher than 4 adequate precision ratios of the models demonstrate that the noise in models is insignificant [178]. All models exhibit high R^2 (>0.9) and show excellent agreement between the predicted and adjusted R^2 (*i.e.* the difference is less than 0.2, which is the commonly used criteria). The resulting relationships between the experimental data relevant to the design points in comparison to RS model predictions are shown in Fig. 11. It can be seen that for all the models (E, σ_c, ε_f, υ and), the values closely follow the best-fit line (diagonal dotted line). This shows that the response surface models represented by the respective equations (2-6) have excellent accuracy in predicting both the mechanical performance and interaction of the design parameters. Accordingly, it can be confirmed that the RS model developed in this study is accurate and valid allowing it to navigate the whole design space (limits of the design variables).

3.4.2. Interaction effects of design variables on E

From Fig. 12a, it can be seen that the elastic modulus depends on both the thickness and angle of the structure in a linear fashion. E increases linearly with an increase in t and θ reaching the highest modulus when both t and θ are at their peak. This shows that the interdependence of the design parameters on E is minimal and does not affect the performance trend. Therefore, for the presented structure, one can increase t irrespective of θ and expect E to increase and *vice versa*. This means that the behaviour is linked to the influence of the design parameters on the relative density. Increasing t increases relative density resulting in more material resisting deformation thus increasing the overall stiffness of the structure. On the other hand, increasing θ pushes the chevron beams further apart reducing the effect of the artificially induced buckling and thus having a higher resistance to deformation resulting in increased stiffness.

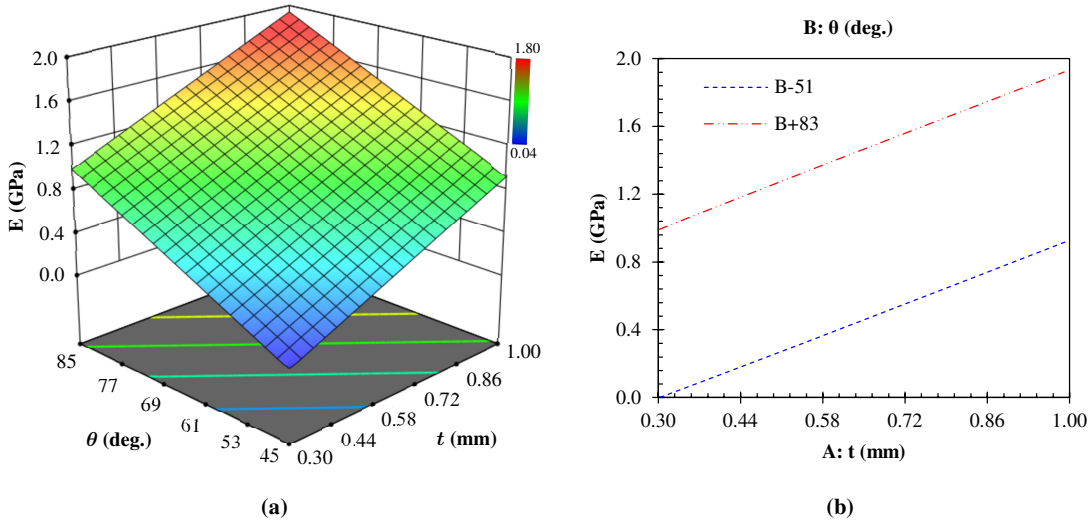

Fig. 12. Influence of the design parameters on the mechanical performance showing **(a)** the interdependence and **(b)** the interaction effects of t and $\boldsymbol{\theta}$ on E.

The limited interaction between the design parameters can be validated by Fig. 11b, where the trend in performance with respect to t is analysed for different θ values. It can appear that the interaction effect between the design parameters is minimal, confirmed through a constant performance slope despite the difference in θ. Overall, the most significant terms on E are the first-order effects of t and θ in the order $t>\theta$ where the thickness has a higher influence in comparison to θ. This means that if the goal is to increase the stiffness, increasing t will yield a higher E in comparison increasing the same amount θ.

3.4.3. Interaction effects of design variables on σ_c

Fig. 13a shows the interdependence of the angle and thickness on the compressive strength of the layer-based re-entrant arrangement. It can be seen that σ_c is highly sensitive to both t and θ, where the strength rises when both of these parameters are increased. The larger the θ and t values, the higher the compressive strength became. An observation also reported by Filho *et al.* [179] while studying traditional beam based auxetic structure with crosslinks in a different material. However, different to what was observed in the case of E (Section 3.4.2), the interaction between the parameters on the resulting σ_c is significant as shown in Fig. 13b.

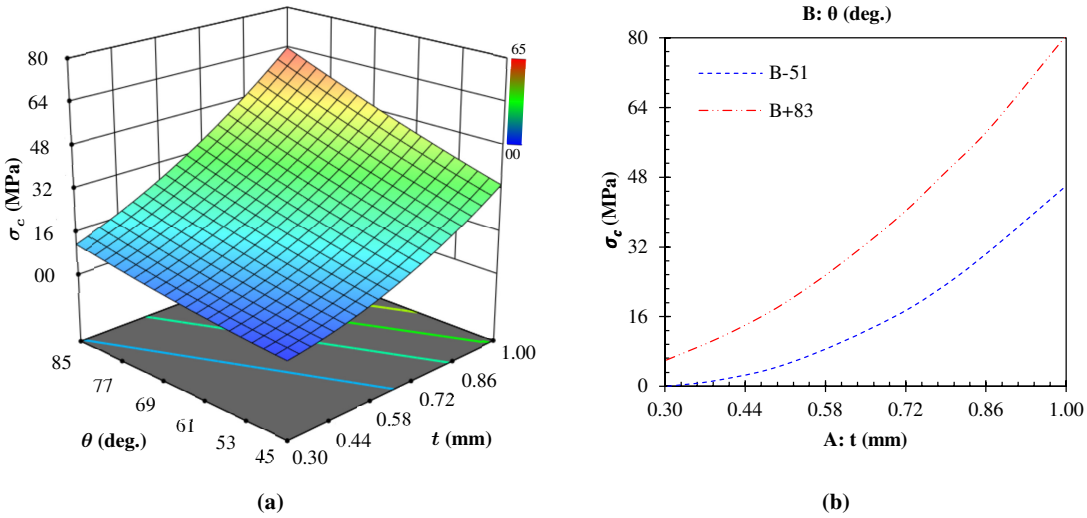

Fig. 13. Influence of the design parameters on the mechanical performance showing **(a)** the interdependence and **(b)** the interaction effects of $\boldsymbol{t}$ and $\boldsymbol{\theta}$ on $\boldsymbol{\sigma_c}$.

It is clear that the influence of t on the compressive strength varies with θ. This can be observed from the difference in the slope of the polynomial curve with respect to t at different θ. Overall, thickness has a higher influence when θ is higher, which means that the interaction effect between the design parameters is significant and needs to be taken into consideration while designing thin and thick-walled auxetic structure. Nevertheless, similar to E, the most significant terms on σ_c are the first-order effects of t and θ in the order $t > \theta$ where the thickness has a significantly higher influence in comparison to θ.

3.4.4. Interaction effects of design variables on ε_f

Fig. 14a shows that the strain at collapse (ε_f) decreased as the thickness increased at angles lower than 78° for the cellular architecture being considered. However, at higher angles (>78°), the failure strain increased drastically with respect to increase in thickness. This shows that when it comes to the effect of the geometrical parameters on the ε_f, the interaction effect is highly significant. While at lower thickness, increasing θ results in reducing ε_f, the opposite was true at higher angles. This trend is clearly visible in Fig. 14b, where a higher angle of 83° almost shows an opposite trend to lower angle (51°).

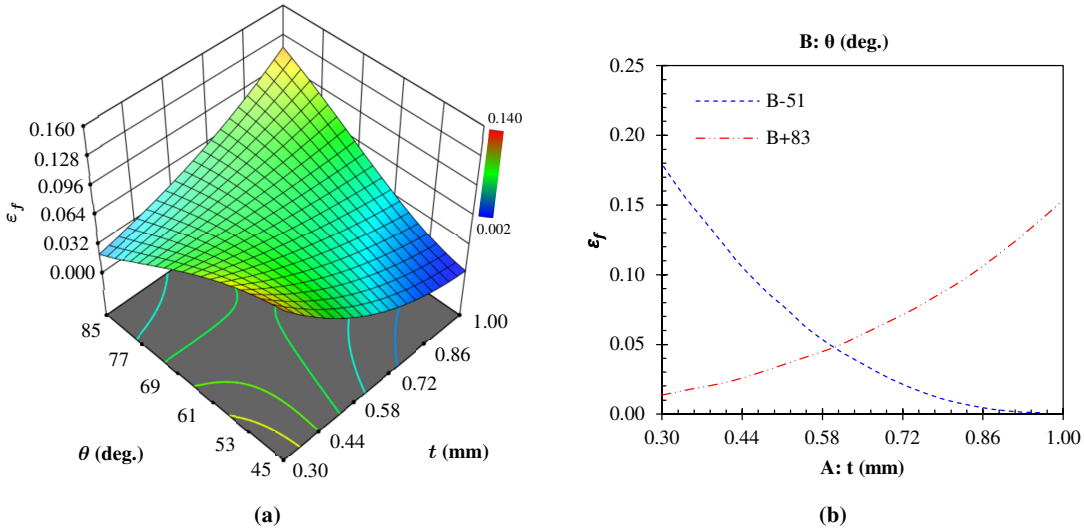

Fig. 14. Influence of the design parameters on the mechanical performance showing **(a)** the interdependence and **(b)** the interaction effects of $\boldsymbol{t}$ and $\boldsymbol{\theta}$ on $\boldsymbol{\varepsilon_f}$.

The reason for this is that at lower angles increasing the thickness reduces the porosity making the structure more dense and stiff resulting in a lower failure strain similar to traditional non-auxetic structures. However, at higher angles increasing the thickness allows preserving a certain porosity due to the larger size of the unit cell itself allowing increased deformation of the walls. Furthermore, thick walls were also free from structural inhomogeneity; a distinctive feature of the SLM process shown in Fig. 6. Overall, the most significant terms on ε_f are the interaction effect followed by the first and second-order effects of t and θ respectively. Consequently, the order of influence of the geometrical parameters when it comes to the failure strain is highly influenced by interaction effects between the geometrical parameters.

3.4.5. Interaction effects of design variables on υ

All the structures derived from varying both t and θ exhibited negative Poisson's ratio despite the absence of the lateral crosslinks connecting the chevron walls. This allows for the evolution of the auxetic structure from a single unit-cell to a layer-based phenomenon. The response surface data shows that both the design parameters have a distinctive role to play in modulating the Poisson's ratio. The absolute value of υ was found to decrease when the thickness increased; a

trend opposite to the case when θ increased. Accordingly, the highest value of $-\upsilon$ was observed at the highest angle and lowest thickness. This is primarily because the structures exhibit negative Poisson's ratio due to the buckling of the chevron walls.

From a mechanical point of view, Poisson's ratio is defined as the negative ratio of the transverse strain to the axial strain. Therefore, in order to exhibit negative υ the material must be allowed to laterally shrink under axial compression in this case. Further to the shape of the unit cell, the amount of porosity or the void space dictates how much a structure can shrink. In this view, increasing the angle is beneficial as this allows more space for the structure to shrink and therefore reach higher negative Poisson's ratio.

On the other hand, increasing the thickness decreases the porosity, which is less conducive to the absolute value of the Poisson's ratio in the negative direction. For the structure under consideration, the angle has a higher significance over θ in dictating the absolute value of the Poisson's ratio. Overall, the most significant terms on $-\upsilon$ are the first-order effect of θ followed by t and then the interaction effect of $t\theta$. Consequently, the order of influence of the geometrical parameters when it comes to the Poisson's ratio is $\theta > t > t\theta > \theta^2$. The effect of t^2 was found to be negligible for the geometrical range considered in this study.

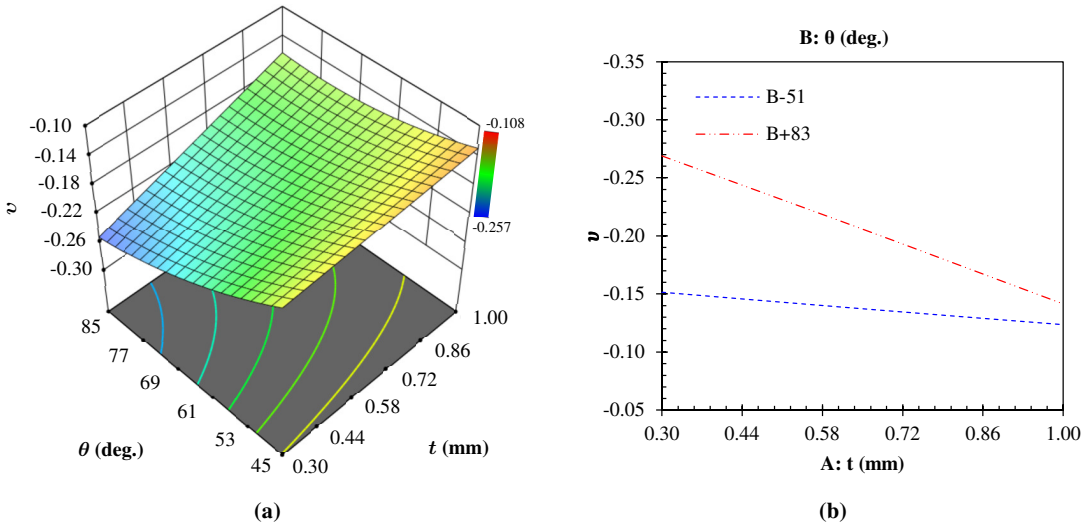

Fig. 15. Influence of the design parameters on the mechanical performance showing **(a)** the interdependence and **(b)** the interaction effects of $\boldsymbol{t}$ and $\boldsymbol{\theta}$ on $\boldsymbol{\upsilon}$.

3.4.6. Interaction effects of design variables on

From Fig. 16a, it can be seen that the relative density depends primarily on the thickness and marginally on the angle of the structure in a linear fashion. increases linearly with an increase in t and decrease in θ, reaching peak density when t and θ are its highest and lowest respectively. This shows that the interdependence of the design parameters on is minimal and does not affect the performance trend as shown in Fig. 16b resulting in a constant performance slope

despite the difference in θ. Therefore, for the presented structure, one can increase t irrespective of θ and expect to increase. Overall, the most significant terms on are the first-order effects of t and θ in the order $t>\theta$ where the thickness has a significantly higher influence in comparison to θ. This means that if the goal is to increase the relative density, increasing t will yield a higher in comparison to decreasing the same amount of θ.

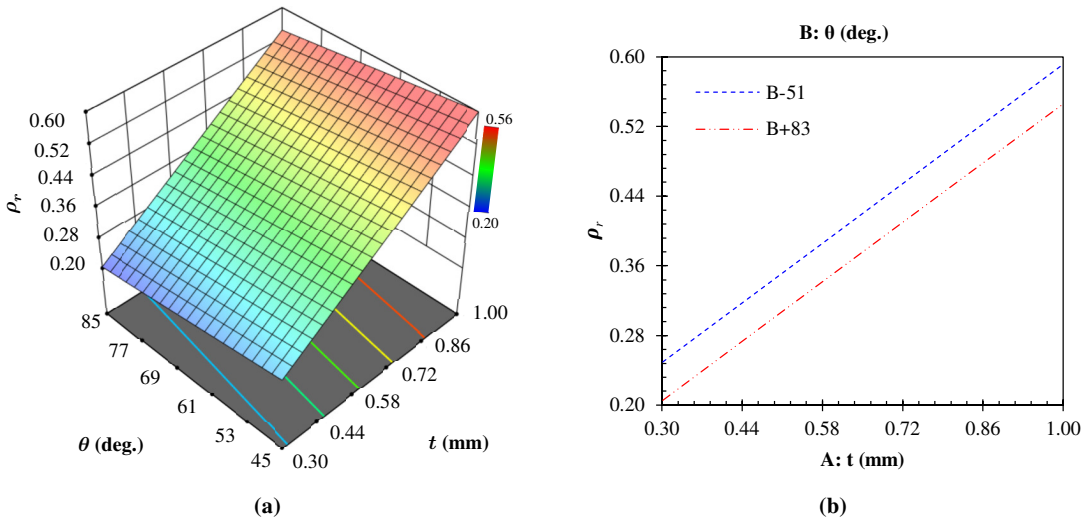

Fig. 16. Influence of the design parameters on the relative density of the structure showing **(a)** the interdependence and **(b)** the interaction effects of $\boldsymbol{t}$ and $\boldsymbol{\theta}$ on $\boldsymbol{\rho_r}$.

Overall, it clear that thin and thick-walled layered re-entrant structures offer new possibilities for targeted multifunctional behaviour and properties at the same time allowing customisability, and scalability. Therefore, it is of vital importance to continue to understand and quantify the typical properties of negative Poisson's ratio materials in order to accurately alter its properties and deformation behaviours for specific applications. It is demonstrated that AlSi10Mg walled re-entrant structure in the absence of a traditional crosslink allows for stable deformation while retaining negative Poisson's ratio in the range of -0.108 to -0.257.

4. Conclusion

Manufacturing techniques capable of exploiting the benefits of complex shapes and sizes are increasingly being used to develop auxetic structures. However, the scalability of the walled variants of traditional beam-based $-\upsilon$ models is challenged due to their unstable behaviour. In this regard, this study demonstrates thin and thick-walled AlSi10Mg layer-based re-entrant architecture featuring stable global deformation at the same time yielding a negative Poisson's ratio of -0.108 to -0.257. The structures were manufactured using SLM, and the results show that the absence of the traditional crosslink allows for the formation of a continuous lateral layer creating an inherently stable structure under quasi-static loading. Nevertheless, the enhanced surface area coupled with the effects of SLM resulted in a certain variation between the relative density between the ideal geometry and SLM prototype for thin-walled samples (0.3 mm) and

overhang angles (45°-85°). The experimentally informed parametric analysis showed that the elastic modulus of the structures increased linearly with increasing t and θ with the former having a higher influence on the rate of increase. Though the same was true for compressive strength, a significant effect of interaction between the geometrical parameters were observed. This meant that the rate of increase in σ_c with respect to increasing t was dependent on the compounding effect of θ. On the other hand, the failure strain was led by the interaction of $t\theta$ (AB) where the performance trajectory (increase *vs* decrease) with respect to t reversed depending upon θ. This allows the creation of tunable ε_f by simply modulating θ irrespective of the wall thickness. The relative density of the structure primarily depends on t and marginally on θ in a linear fashion. increases linearly with an increase in t and decrease in θ, with the most significant terms being the first-order effects of t and θ in the order $t>\theta$. Lastly, the most significant terms on Poisson's ratio was found to be the first-order effect of θ followed by t and then the interaction effect of $t\theta$ leading to an order of influence of $\theta>t>t\theta>\theta^2$. However, the second-order influence of t^2 on the Poisson's ratio was found to be negligible for the geometrical range conceived at $0.3 \leq t \leq 1$ mm and $45° \leq \theta \leq 85°$. Overall, the study suggests that stable mechanical performance of thin and thick-walled $-\upsilon$ structures can be enhanced by layer-based arrangement and the careful selection of the design parameters t and θ. The design and analysis philosophy conceived in this study allows altering the properties of thin and thick-walled re-entrant structures conventionally known to exhibit unexpected mechanical properties and unstable lateral deformation, enhancing its potential for multifunctional applications.

Data availability

The data that support the findings of this study are available from the corresponding author upon reasonable request.

References

[1] K.E. Evans, Auxetic polymers: a new range of materials, Endeavour. 15 (1991) 170–174. https://doi.org/10.1016/0160-9327(91)90123-S.

[2] M.-J. Choi, S.-H. Kang, M.-H. Oh, S. Cho, Controllable optimal design of auxetic structures for extremal Poisson's ratio of −2, Compos. Struct. 226 (2019) 111215. https://doi.org/10.1016/J.COMPSTRUCT.2019.111215.

[3] M.J. Mirzaali, A. Caracciolo, H. Pahlavani, S. Janbaz, L. Vergani, A.A. Zadpoor, Multi-material 3D printed mechanical metamaterials: Rational design of elastic properties through spatial distribution of hard and soft phases, Appl. Phys. Lett. 113 (2018) 241903. https://doi.org/10.1063/1.5064864.

[4] M.J. Mirzaali, H. Pahlavani, A.A. Zadpoor, Auxeticity and stiffness of random networks: Lessons for the rational design of 3D printed mechanical metamaterials, Appl. Phys. Lett. 115 (2019) 021901. https://doi.org/10.1063/1.5096590.

[5] K.W. Wojciechowski, Remarks on "Poisson ratio beyond the limits of the elasticity theory," J. Phys. Soc. Japan. 72 (2003) 1819–1820. https://doi.org/10.1143/JPSJ.72.1819.

[6] S. Jin, Y.P. Korkolis, Y. Li, Shear resistance of an auxetic chiral mechanical metamaterial, Int. J. Solids Struct. 174–175 (2019) 28–37. https://doi.org/10.1016/J.IJSOLSTR.2019.06.005.

[7] A.R. El Dhaba, M. Shaat, Modeling deformation of auxetic and non-auxetic polymer gels, Appl. Math. Model. 74 (2019) 320–336. https://doi.org/10.1016/J.APM.2019.04.050.

[8] I. Shufrin, E. Pasternak, A. V. Dyskin, Effective properties of layered auxetic hybrids, Compos. Struct. 209 (2019) 391–400. https://doi.org/10.1016/J.COMPSTRUCT.2018.10.072.

[9] S. Jeong, H.H. Yoo, Shape optimization of bowtie-shaped auxetic structures using beam theory, Compos. Struct. 224 (2019) 111020. https://www.sciencedirect.com/science/article/pii/S0263822319309377 (accessed September 19, 2019).

[10] H. Wang, Z. Lu, Z. Yang, X. Li, A novel re-entrant auxetic honeycomb with enhanced in-plane impact resistance, Compos. Struct. 208 (2019) 758–770. https://doi.org/10.1016/J.COMPSTRUCT.2018.10.024.

[11] W. Lee, Y. Jeong, J. Yoo, H. Huh, S.-J. Park, S.H. Park, J. Yoon, Effect of auxetic structures on crash behavior of cylindrical tube, Compos. Struct. 208 (2019) 836–846. https://doi.org/10.1016/J.COMPSTRUCT.2018.10.068.

[12] G. Imbalzano, S. Linforth, T.D. Ngo, P.V.S. Lee, P. Tran, Blast resistance of auxetic and honeycomb sandwich panels: Comparisons and parametric designs, Compos. Struct. 183 (2018) 242–261. https://doi.org/10.1016/J.COMPSTRUCT.2017.03.018.

[13] S. Hou, T. Li, Z. Jia, L. Wang, Mechanical properties of sandwich composites with 3d-printed auxetic and non-auxetic lattice cores under low velocity impact, Mater. Des. 160 (2018) 1305–1321. https://doi.org/10.1016/J.MATDES.2018.11.002.

[14] H. Nikkhah, A. Baroutaji, Z. Kazancı, A. Arjunan, Evaluation of crushing and energy absorption characteristics of bio-inspired nested structures, Thin-Walled Struct. 148 (2020) 106615. https://doi.org/10.1016/j.tws.2020.106615.

[15] L.L. Hu, M.Z. Zhou, H. Deng, Dynamic indentation of auxetic and non-auxetic honeycombs under large deformation, Compos. Struct. 207 (2019) 323–330. https://doi.org/10.1016/J.COMPSTRUCT.2018.09.066.

[16] On the conical indentation response of elastic auxetic materials: Effects of Poisson's ratio, contact friction and cone angle, Int. J. Solids Struct. 81 (2016) 33–42. https://doi.org/10.1016/J.IJSOLSTR.2015.10.020.

[17] N. Chan, K.E. Evans, Indentation Resilience of Conventional and Auxetic Foams, J. Cell. Plast. 34 (1998) 231–260. https://doi.org/10.1177/0021955X9803400304.

[18] T.-C. Lim, Contact and Indentation Mechanics of Auxetic Materials, in: Springer, Singapore, 2015: pp. 171–199. https://doi.org/10.1007/978-981-287-275-3_5.

[19] J.B. Choi, R.S. Lakes, Fracture toughness of re-entrant foam materials with a negative Poisson's ratio: experiment and analysis, Int. J. Fract. 80 (1996) 73–83. https://doi.org/10.1007/BF00036481.

[20] J.P. Donoghue, K.L. Alderson, K.E. Evans, The fracture toughness of composite laminates with a negative Poisson's ratio, Phys. Status Solidi. 246 (2009) 2011–2017. https://doi.org/10.1002/pssb.200982031.

[21] B. Nečemer, J. Kramberger, S. Glodež, Fatigue crack initiation and propagation in auxetic porous structures, Procedia Struct. Integr. 13 (2018) 2261–2266. https://doi.org/10.1016/J.PROSTR.2018.12.130.

[22] A.S. Praveen, A. Arjunan, Effect of nano-Al2O3 addition on the microstructure and erosion wear of HVOF sprayed NiCrSiB coatings, Mater. Res. Express. 7 (2019) 015006. https://doi.org/10.1088/2053-1591/ab5bda.

[23] M. Bianchi, F. Scarpa, Vibration transmissibility and damping behaviour for auxetic and conventional foams under linear and nonlinear regimes, Smart Mater. Struct. 22 (2013) 084010. https://doi.org/10.1088/0964-1726/22/8/084010.

[24] L. Ma, Y.-L. Chen, J.-S. Yang, X.-T. Wang, G.-L. Ma, R. Schmidt, K.-U. Schröder, Modal characteristics and damping enhancement of carbon fiber composite auxetic double-arrow corrugated sandwich panels, Compos. Struct. 203 (2018) 539–550. https://doi.org/10.1016/J.COMPSTRUCT.2018.07.006.

[25] N.D. Duc, K. Seung-Eock, N.D. Tuan, P. Tran, N.D. Khoa, New approach to study nonlinear dynamic response and vibration of sandwich composite cylindrical panels with auxetic honeycomb core layer, Aerosp. Sci. Technol. 70 (2017) 396–404. https://doi.org/10.1016/J.AST.2017.08.023.

[26] X. Ren, J. Shen, P. Tran, T.D. Ngo, Y.M. Xie, Auxetic nail: Design and experimental study, Compos. Struct. 184 (2018) 288–298. https://doi.org/10.1016/J.COMPSTRUCT.2017.10.013.

[27] L. Peel, M. Abdelrahman, Studying the Physical Properties and Auxetic Behavior of 3D-printed Fasteners, in: ASEE Annu. Conf. Expo. San Antonio, Texas., 2012: pp. 25.1204.1-25.1204.12. https://peer.asee.org/studying-the-physical-properties-and-auxetic-behavior-of-3d-printed-fasteners (accessed September 19, 2019).

[28] S. Mohsenizadeh, Z. Ahmad, Auxeticity effect on crushing characteristics of auxetic foam-filled square tubes under axial loading, Thin-Walled Struct. 145 (2019) 106379. https://doi.org/10.1016/J.TWS.2019.106379.

[29] M.F. Ahmed, Y. Li, C. Zeng, Stretchable and compressible piezoresistive sensors from auxetic foam and silver nanowire, Mater. Chem. Phys. 229 (2019) 167–173. https://doi.org/10.1016/J.MATCHEMPHYS.2019.03.015.

[30] T. Zahra, M. Dhanasekar, Characterisation of cementitious polymer mortar – Auxetic foam composites, Constr. Build. Mater. 147 (2017) 143–159. https://doi.org/10.1016/J.CONBUILDMAT.2017.04.151.

[31] Y. Yao, Y. Luo, Y. Xu, B. Wang, J. Li, H. Deng, H. Lu, Fabrication and characterization of auxetic shape memory composite foams, Compos. Part B Eng. 152 (2018) 1–7. https://doi.org/10.1016/J.COMPOSITESB.2018.06.027.

[32] X. Zhai, J. Gao, H. Liao, C.D. Kirk, Y.A. Balogun, W.W. Chen, Mechanical behaviors of auxetic polyurethane foam at quasi-static, intermediate and high strain rates, Int. J. Impact Eng. 129 (2019) 112–118. https://doi.org/10.1016/J.IJIMPENG.2019.03.002.

[33] F. Najarian, R. Alipour, M. Shokri Rad, A.F. Nejad, A. Razavykia, Multi-objective optimization of converting process of auxetic foam using three different statistical methods, Measurement. 119 (2018) 108–116. https://doi.org/10.1016/J.MEASUREMENT.2018.01.064.

[34] A. Arjunan, A. Baroutaji, A.S. Praveen, A.G. Olabi, C.J. Wang, Acoustic Performance of Metallic Foams, in: Ref. Modul. Mater. Sci. Mater. Eng., Elsevier, 2019. https://doi.org/10.1016/B978-0-12-803581-8.11561-9.

[35] Y. Yan, Y. Li, L. Song, C. Zeng, Y. Li, Pluripotent stem cell expansion and neural differentiation in 3-D scaffolds of tunable Poisson's ratio, Acta Biomater. 49 (2017) 192–203. https://doi.org/10.1016/J.ACTBIO.2016.11.025.

[36] H.M.A. Kolken, S. Janbaz, S.M.A. Leeflang, K. Lietaert, H.H. Weinans, A.A. Zadpoor, Rationally designed meta-implants: a combination of auxetic and conventional meta-biomaterials, Mater. Horizons. 5 (2018) 28–35. https://doi.org/10.1039/C7MH00699C.

[37] F.S.L. Bobbert, S. Janbaz, A.A. Zadpoor, Towards deployable meta-implants, J. Mater. Chem. B. 6 (2018) 3449–3455. https://doi.org/10.1039/c8tb00576a.

[38] A. Arjunan, M. Demetriou, A. Baroutaji, C. Wang, Mechanical performance of highly permeable laser melted Ti6Al4V bone scaffolds, J. Mech. Behav. Biomed. Mater. 102 (2020). https://doi.org/10.1016/j.jmbbm.2019.103517.

[39] J. Ou, Z. Ma, J. Peters, S. Dai, N. Vlavianos, H. Ishii, KinetiX - designing auxetic-inspired deformable material structures, Comput. Graph. 75 (2018) 72–81. https://doi.org/10.1016/J.CAG.2018.06.003.

[40] A. Amendola, F. Fraternali, Incremental auxetic response of composite lattices under isotropic prestress, Compos. Struct. 191 (2018) 145–153. https://doi.org/10.1016/J.COMPSTRUCT.2018.02.020.

[41] S. Yuan, F. Shen, J. Bai, C.K. Chua, J. Wei, K. Zhou, 3D soft auxetic lattice structures fabricated by selective laser sintering: TPU powder evaluation and process optimization, Mater. Des. 120 (2017) 317–327.

https://doi.org/10.1016/J.MATDES.2017.01.098.

[42] B. Ling, K. Wei, Z. Wang, X. Yang, Z. Qu, D. Fang, Experimentally program large magnitude of Poisson's ratio in additively manufactured mechanical metamaterials, Int. J. Mech. Sci. 173 (2020). https://doi.org/10.1016/j.ijmecsci.2020.105466.

[43] S. Duan, L. Xi, W. Wen, D. Fang, A novel design method for 3D positive and negative Poisson's ratio material based on tension-twist coupling effects, Compos. Struct. 236 (2020). https://doi.org/10.1016/j.compstruct.2020.111899.

[44] V.H. Carneiro, H. Puga, J. Meireles, Positive, zero and negative Poisson's ratio non-stochastic metallic cellular solids: Dependence between static and dynamic mechanical properties, Compos. Struct. 226 (2019) 111239. https://doi.org/10.1016/j.compstruct.2019.111239.

[45] H. Wang, Y. Zhang, W. Lin, Q.-H. Qin, A novel two-dimensional mechanical metamaterial with negative Poisson's ratio, Comput. Mater. Sci. 171 (2020) 109232. https://doi.org/10.1016/j.commatsci.2019.109232.

[46] Q. Gao, C.A. Tan, G. Hulbert, L. Wang, Geometrically nonlinear mechanical properties of auxetic double-V microstructures with negative Poisson's ratio, Eur. J. Mech. A/Solids. 80 (2020). https://doi.org/10.1016/j.euromechsol.2019.103933.

[47] J.A. Harris, G.J. McShane, Metallic stacked origami cellular materials: Additive manufacturing, properties, and modelling, Int. J. Solids Struct. 185–186 (2020) 448–466. https://doi.org/10.1016/j.ijsolstr.2019.09.007.

[48] H. Zong, H. Zhang, Y. Wang, M.Y. Wang, J.Y.H. Fuh, On two-step design of microstructure with desired Poisson's ratio for AM, Mater. Des. 159 (2018) 90–102. https://doi.org/10.1016/j.matdes.2018.08.032.

[49] C. Li, H.S. Shen, H. Wang, Postbuckling behavior of sandwich plates with functionally graded auxetic 3D lattice core, Compos. Struct. 237 (2020). https://doi.org/10.1016/j.compstruct.2020.111894.

[50] X. Li, L. Gao, W. Zhou, Y. Wang, Y. Lu, Novel 2D metamaterials with negative Poisson's ratio and negative thermal expansion, Extrem. Mech. Lett. 30 (2019). https://doi.org/10.1016/j.eml.2019.100498.

[51] A. Spagnoli, R. Brighenti, M. Lanfranchi, F. Soncini, On the Auxetic Behaviour of Metamaterials with Re-entrant Cell Structures, Procedia Eng. 109 (2015) 410–417. https://doi.org/10.1016/J.PROENG.2015.06.252.

[52] H. Lekesiz, S.K. Bhullar, A.A. Karaca, M.B.G. Jun, Mechanical characterization of auxetic stainless steel thin sheets with reentrant structure, Smart Mater. Struct. 26 (2017) 085022. https://doi.org/10.1088/1361-665X/aa73a4.

[53] A. Alomarah, D. Ruan, S. Masood, Tensile properties of an auxetic structure with re-entrant and chiral features—a finite element study, Int. J. Adv. Manuf. Technol. 99 (2018) 2425–2440. https://doi.org/10.1007/s00170-018-2637-y.

[54] Y. Jiang, B. Rudra, J. Shim, Y. Li, Limiting strain for auxeticity under large compressive Deformation: Chiral vs. re-entrant cellular solids, Int. J. Solids Struct. 162 (2019) 87–95. https://doi.org/10.1016/J.IJSOLSTR.2018.11.035.

[55] T. Wang, L. Wang, Z. Ma, G.M. Hulbert, Elastic analysis of auxetic cellular structure consisting of re-entrant hexagonal cells using a strain-based expansion homogenization method, Mater. Des. 160 (2018) 284–293. https://doi.org/10.1016/J.MATDES.2018.09.013.

[56] B. Nečemer, J. Kramberger, T. Vuherer, S. Glodež, Fatigue crack initiation and propagation in re-entrant auxetic cellular structures, Int. J. Fatigue. 126 (2019) 241–247. https://doi.org/10.1016/J.IJFATIGUE.2019.05.010.

[57] Y. Jiang, Y. Li, 3D Printed Auxetic Mechanical Metamaterial with Chiral Cells and Re-entrant Cores, Sci. Rep. 8 (2018) 2397. https://doi.org/10.1038/s41598-018-20795-2.

[58] S.C. Han, D.S. Kang, K. Kang, Two nature-mimicking auxetic materials with potential for high energy

absorption, Mater. Today. 26 (2019) 30–39. https://doi.org/10.1016/j.mattod.2018.11.004.

[59] H.M.A. Kolken, A.A. Zadpoor, Auxetic mechanical metamaterials, RSC Adv. 7 (2017) 5111–5129. https://doi.org/10.1039/C6RA27333E.

[60] K.W. Wojciechowski, Two-dimensional isotropic system with a negative poisson ratio, Phys. Lett. A. 137 (1989) 60–64. https://doi.org/10.1016/0375-9601(89)90971-7.

[61] K.W. Wojciechowski, Constant thermodynamic tension Monte Carlo studies of elastic properties of a two-dimensional system of hard cyclic hexamers, Mol. Phys. 61 (1987) 1247–1258. https://doi.org/10.1080/00268978700101761.

[62] L. Mizzi, D. Attard, R. Gatt, A.A. Pozniak, K.W. Wojciechowski, J.N. Grima, Influence of translational disorder on the mechanical properties of hexachiral honeycomb systems, (2015). https://doi.org/10.1016/j.compositesb.2015.04.057.

[63] J.N. Grima, E. Chetcuti, E. Manicaro, D. Attard, M. Camilleri, R. Gatt, K.E. Evans, On the auxetic properties of generic rotating rigid triangles, Proc. R. Soc. A Math. Phys. Eng. Sci. 468 (2012) 810–830. https://doi.org/10.1098/rspa.2011.0273.

[64] K.K. Dudek, R. Gatt, L. Mizzi, M.R. Dudek, D. Attard, K.E. Evans, J.N. Grima, On the dynamics and control of mechanical properties of hierarchical rotating rigid unit auxetics, Sci. Rep. 7 (2017) 46529. https://doi.org/10.1038/srep46529.

[65] D. Attard, A. Casha, J. Grima, Filtration Properties of Auxetics with Rotating Rigid Units, Materials (Basel). 11 (2018) 725. https://doi.org/10.3390/ma11050725.

[66] A. Alderson, K.L. Alderson, D. Attard, K.E. Evans, R. Gatt, J.N. Grima, W. Miller, N. Ravirala, C.W. Smith, K. Zied, Elastic constants of 3-, 4- and 6-connected chiral and anti-chiral honeycombs subject to uniaxial in-plane loading, Compos. Sci. Technol. 70 (2010) 1042–1048. https://doi.org/10.1016/j.compscitech.2009.07.009.

[67] A.A. Pozniak, K.W. Wojciechowski, Poisson's ratio of rectangular anti-chiral structures with size dispersion of circular nodes, Phys. Status Solidi. 251 (2014) 367–374. https://doi.org/10.1002/pssb.201384256.

[68] L. Rothenburg, A.A. Berlin, R.J. Bathurst, Microstructure of isotropic materials with negative Poisson's ratio, Nature. 354 (1991) 470–472. https://doi.org/10.1038/354470a0.

[69] R. Lakes, K.W. Wojciechowski, Negative compressibility, negative Poisson's ratio, and stability, Phys. Status Solidi. 245 (2008) 545–551. https://doi.org/10.1002/pssb.200777708.

[70] A.A. Poźniak, K.W. Wojciechowski, J.N. Grima, L. Mizzi, Planar auxeticity from elliptic inclusions, Compos. Part B Eng. 94 (2016) 379–388. https://doi.org/10.1016/j.compositesb.2016.03.003.

[71] M. Bilski, K.W. Wojciechowski, Tailoring Poisson's ratio by introducing auxetic layers, Phys. Status Solidi. 253 (2016) 1318–1323. https://doi.org/10.1002/pssb.201600140.

[72] A.A. Zadpoor, Mechanical performance of additively manufactured meta-biomaterials, Acta Biomater. 85 (2019) 41–59. https://doi.org/10.1016/j.actbio.2018.12.038.

[73] Q. Gao, C. Ge, W. Zhuang, L. Wang, Z. Ma, Crashworthiness analysis of double-arrowed auxetic structure under axial impact loading, Mater. Des. 161 (2019) 22–34. https://doi.org/10.1016/J.MATDES.2018.11.013.

[74] E. Khare, S. Temple, I. Tomov, F. Zhang, S.K. Smoukov, Low Fatigue Dynamic Auxetic Lattices With 3D Printable, Multistable, and Tuneable Unit Cells, Front. Mater. 5 (2018) 45. https://doi.org/10.3389/fmats.2018.00045.

[75] H. Yang, B. Wang, L. Ma, Mechanical properties of 3D double-U auxetic structures, Int. J. Solids Struct. 180–181 (2019) 13–29. https://www.sciencedirect.com/science/article/pii/S002076831930318X (accessed September 19, 2019).

[76] L. Yang, O. Harrysson, H. West, D. Cormier, Mechanical properties of 3D re-entrant honeycomb auxetic structures realized via additive manufacturing, Int. J. Solids Struct. 69–70 (2015) 475–490. https://doi.org/10.1016/J.IJSOLSTR.2015.05.005.

[77] R. Gatt, L. Mizzi, J.I. Azzopardi, K.M. Azzopardi, D. Attard, A. Casha, J. Briffa, J.N. Grima, Hierarchical Auxetic Mechanical Metamaterials, Sci. Rep. 5 (2015) 8395. https://doi.org/10.1038/srep08395.

[78] Y. Tang, J. Yin, Design of cut unit geometry in hierarchical kirigami-based auxetic metamaterials for high stretchability and compressibility, Extrem. Mech. Lett. 12 (2017) 77–85. https://doi.org/10.1016/J.EML.2016.07.005.

[79] N. Ejiri, T. Shoda, Stability of triply periodic minimal surfaces, Differ. Geom. Its Appl. 67 (2019) 101555. https://doi.org/10.1016/J.DIFGEO.2019.101555.

[80] S.J.P. Callens, N. Tümer, A.A. Zadpoor, Hyperbolic origami-inspired folding of triply periodic minimal surface structures, Appl. Mater. Today. 15 (2019) 453–461. https://doi.org/10.1016/j.apmt.2019.03.007.

[81] L. Yang, M. Ferrucci, R. Mertens, W. Dewulf, C. Yan, Y. Shi, S. Yang, An investigation into the effect of gradients on the manufacturing fidelity of triply periodic minimal surface structures with graded density fabricated by selective laser melting, J. Mater. Process. Technol. 275 (2020) 116367. https://doi.org/10.1016/J.JMATPROTEC.2019.116367.

[82] L. Yang, C. Yan, C. Han, P. Chen, S. Yang, Y. Shi, Mechanical response of a triply periodic minimal surface cellular structures manufactured by selective laser melting, Int. J. Mech. Sci. 148 (2018) 149–157. https://doi.org/10.1016/J.IJMECSCI.2018.08.039.

[83] T. Maconachie, M. Leary, B. Lozanovski, X. Zhang, M. Qian, O. Faruque, M. Brandt, SLM lattice structures: Properties, performance, applications and challenges6, Mater. Des. 183 (2019) 108137. https://doi.org/10.1016/J.MATDES.2019.108137.

[84] Z. Wang, Recent advances in novel metallic honeycomb structure, Compos. Part B Eng. 166 (2019) 731–741. https://doi.org/10.1016/J.COMPOSITESB.2019.02.011.

[85] H. Hu, M. Zhang, Y. Liu, H. Hu, M. Zhang, Y. Liu, Auxetic structures and mechanisms, Auxetic Text. (2019) 19–56. https://doi.org/10.1016/B978-0-08-102211-5.00002-4.

[86] X. Li, Q. Wang, Z. Yang, Z. Lu, Novel auxetic structures with enhanced mechanical properties, Extrem. Mech. Lett. 27 (2019) 59–65. https://doi.org/10.1016/J.EML.2019.01.002.

[87] L. Jiang, H. Hu, Low-velocity impact response of multilayer orthogonal structural composite with auxetic effect, Compos. Struct. 169 (2017) 62–68. https://doi.org/10.1016/J.COMPSTRUCT.2016.10.018.

[88] S. Yang, V.B. Chalivendra, Y.K. Kim, Fracture and impact characterization of novel auxetic Kevlar®/Epoxy laminated composites, Compos. Struct. 168 (2017) 120–129. https://doi.org/10.1016/J.COMPSTRUCT.2017.02.034.

[89] K. Billon, I. Zampetakis, F. Scarpa, M. Ouisse, E. Sadoulet-Reboul, M. Collet, A. Perriman, A. Hetherington, Mechanics and band gaps in hierarchical auxetic rectangular perforated composite metamaterials, Compos. Struct. 160 (2017) 1042–1050. https://doi.org/10.1016/J.COMPSTRUCT.2016.10.121.

[90] M.-H. Fu, Y. Chen, L.-L. Hu, Bilinear elastic characteristic of enhanced auxetic honeycombs, Compos. Struct. 175 (2017) 101–110. https://doi.org/10.1016/J.COMPSTRUCT.2017.04.007.

[91] W. Wu, X. Song, J. Liang, R. Xia, G. Qian, D. Fang, Mechanical properties of anti-tetrachiral auxetic stents, Compos. Struct. 185 (2018) 381–392. https://doi.org/10.1016/J.COMPSTRUCT.2017.11.048.

[92] V.A. Gorodtsov, D.S. Lisovenko, T.-C. Lim, Three-layered plate exhibiting auxeticity based on stretching and bending modes, Compos. Struct. 194 (2018) 643–651. https://doi.org/10.1016/J.COMPSTRUCT.2018.03.092.

[93] K. El Nady, F. Dos Reis, J.F. Ganghoffer, Computation of the homogenized nonlinear elastic response of 2D and 3D auxetic structures based on micropolar continuum models, Compos. Struct. 170 (2017) 271–290. https://doi.org/10.1016/J.COMPSTRUCT.2017.02.043.

[94] J. Smardzewski, D. Jasińska, M. Janus-Michalska, Structure and properties of composite seat with auxetic springs, Compos. Struct. 113 (2014) 354–361. https://doi.org/10.1016/J.COMPSTRUCT.2014.03.041.

[95] M. Assidi, J.-F. Ganghoffer, Composites with auxetic inclusions showing both an auxetic behavior and enhancement of their mechanical properties, Compos. Struct. 94 (2012) 2373–2382. https://doi.org/10.1016/J.COMPSTRUCT.2012.02.026.

[96] Z.-P. Wang, L.H. Poh, Optimal form and size characterization of planar isotropic petal-shaped auxetics with tunable effective properties using IGA, Compos. Struct. 201 (2018) 486–502. https://doi.org/10.1016/J.COMPSTRUCT.2018.06.042.

[97] A. Alderson, K.E. Evans, Modelling concurrent deformation mechanisms in auxetic microporous polymers A 2D model for the deformation of auxetic microporous polymers (those with a negative, 1997. https://search.proquest.com/openview/ce206c9a2fa95f1d8ff4146fc8e0b8a7/1?cbl=2043599&pq-origsite=gscholar (accessed September 20, 2019).

[98] J. Crespo, F.J. Montáns, A continuum approach for the large strain finite element analysis of auxetic materials, Int. J. Mech. Sci. 135 (2018) 441–457. https://doi.org/10.1016/J.IJMECSCI.2017.11.038.

[99] N. Easey, D. Chuprynyuk, W.M.S.W. Musa, A. Bangs, Y. Dobah, A. Shterenlikht, F. Scarpa, Dome-Shape Auxetic Cellular Metamaterials: Manufacturing, Modeling, and Testing, Front. Mater. 6 (2019) 86. https://doi.org/10.3389/fmats.2019.00086.

[100] J.J. Williams, C.W. Smith, K.E. Evans, Z.A.D. Lethbridge, R.I. Walton, An analytical model for producing negative Poisson's ratios and its application in explaining off-axis elastic properties of the NAT-type zeolites, Acta Mater. 55 (2007) 5697–5707. https://doi.org/10.1016/j.actamat.2007.06.011.

[101] P.S. Theocaris, G.E. Stavroulakis, P.D. Panagiotopoulos, Negative Poisson's ratios in composites with star-shaped inclusions: a numerical homogenization approach, Arch. Appl. Mech. (Ingenieur Arch. 67 (1997) 274–286. https://doi.org/10.1007/s004190050117.

[102] J.N. Grima, K.E. Evans, Auxetic behavior from rotating triangles, J. Mater. Sci. 41 (2006) 3193–3196. https://doi.org/10.1007/s10853-006-6339-8.

[103] J. Zeng, H. Cao, H. Hu, Finite element simulation of an auxetic plied yarn structure, Text. Res. J. 89 (2019) 3394–3400. https://doi.org/10.1177/0040517518813659.

[104] G.C. Qiang, Q. Gao, L. Wang, Dynamic Crushing Behaviors of Four Kinds of Auxetic Structures, in: 2019. https://doi.org/10.4271/2019-01-1096.

[105] H. Bahaloo, Y. Li, Micropolar Modeling of Auxetic Chiral Lattices With Tunable Internal Rotation, J. Appl. Mech. 86 (2019). https://doi.org/10.1115/1.4042428.

[106] W.G. Hoover, C.G. Hoover, Searching for auxetics with DYNA3D and ParaDyn, Phys. Status Solidi. 242 (2005) 585–594. https://doi.org/10.1002/pssb.200460377.

[107] M.S. Rad, H. Hatami, Z. Ahmad, A.K. Yasuri, Analytical solution and finite element approach to the dense re-entrant unit cells of auxetic structures, Acta Mech. 230 (2019) 2171–2185. https://doi.org/10.1007/s00707-019-02387-x.

[108] T. Strek, B. Maruszewski, J.W. Narojczyk, K.W. Wojciechowski, Finite element analysis of auxetic plate deformation, J. Non. Cryst. Solids. 354 (2008) 4475–4480. https://doi.org/10.1016/J.JNONCRYSOL.2008.06.087.

[109] A.A. Javadi, A. Faramarzi, R. Farmani, Design and optimization of microstructure of auxetic materials, Eng. Comput. 29 (2012) 260–276. https://doi.org/10.1108/02644401211212398.

[110] D. Li, L. Dong, R.S. Lakes, A unit cell structure with tunable Poisson's ratio from positive to negative, Mater. Lett. 164 (2016) 456–459. https://doi.org/10.1016/J.MATLET.2015.11.037.

[111] C.-Y. Wang, W.-W. Wang, W.-Z. Zhao, Y.-F. Li, G. Zhou, Reliability optimization of a novel negative Poisson's ratio forepart for pedestrian protection, Proc. Inst. Mech. Eng. Part C J. Mech. Eng. Sci. 232 (2018) 2998–3012. https://doi.org/10.1177/0954406217730441.

[112] S. Cui, B. Gong, Q. Ding, Y. Sun, F. Ren, X. Liu, Q. Yan, H. Yang, X. Wang, B. Song, Mechanical Metamaterials Foams with Tunable Negative Poisson's Ratio for Enhanced Energy Absorption and Damage Resistance, Materials (Basel). 11 (2018) 1869. https://doi.org/10.3390/ma11101869.

[113] D. Zhang, J. Xiao, W. Yu, Q. Guo, J. Yang, Hierarchical metal/polymer metamaterials of tunable negative Poisson's ratio fabricated by initiator-integrated 3D printing (i3DP), Nanotechnology. 29 (2018) 505704. https://doi.org/10.1088/1361-6528/aae283.

[114] M. Lei, W. Hong, Z. Zhao, C. Hamel, M. Chen, H. Lu, H.J. Qi, 3D Printing of Auxetic Metamaterials with Digitally Reprogrammable Shape, ACS Appl. Mater. Interfaces. 11 (2019) 22768–22776. https://doi.org/10.1021/acsami.9b06081.

[115] N.E. Uzan, B. Ratzker, P. Landau, S. Kalabukhov, N. Frage, Compressive creep of AlSi10Mg parts produced by selective laser melting additive manufacturing technology, Addit. Manuf. 29 (2019) 100788. https://doi.org/10.1016/J.ADDMA.2019.100788.

[116] D. Agius, K.I. Kourousis, C. Wallbrink, D. Agius, K.I. Kourousis, C. Wallbrink, A Review of the As-Built SLM Ti-6Al-4V Mechanical Properties towards Achieving Fatigue Resistant Designs, Metals (Basel). 8 (2018) 75. https://doi.org/10.3390/met8010075.

[117] Z. Dong, X. Zhang, W. Shi, H. Zhou, H. Lei, J. Liang, Study of Size Effect on Microstructure and Mechanical Properties of AlSi10Mg Samples Made by Selective Laser Melting., Mater. (Basel, Switzerland). 11 (2018). https://doi.org/10.3390/ma11122463.

[118] F. Calignano, Investigation of the accuracy and roughness in the laser powder bed fusion process, Virtual Phys. Prototyp. 13 (2018) 97–104. https://doi.org/10.1080/17452759.2018.1426368.

[119] D. Xiao, X. Chen, Y. Li, W. Wu, D. Fang, The structure response of sandwich beams with metallic auxetic honeycomb cores under localized impulsive loading-experiments and finite element analysis, Mater. Des. 176 (2019) 107840. https://doi.org/10.1016/j.matdes.2019.107840.

[120] L. Geng, W. Wu, L. Sun, D. Fang, Damage characterizations and simulation of selective laser melting fabricated 3D re-entrant lattices based on in-situ CT testing and geometric reconstruction, Int. J. Mech. Sci. 157–158 (2019) 231–242. https://doi.org/https://doi.org/10.1016/j.ijmecsci.2019.04.054.

[121] K. Meena, S. Singamneni, A new auxetic structure with significantly reduced stress concentration effects, Mater. Des. 173 (2019) 107779. https://doi.org/10.1016/J.MATDES.2019.107779.

[122] B. Nagarajan, Z. Hu, X. Song, W. Zhai, J. Wei, Development of Micro Selective Laser Melting: The State of the Art and Future Perspectives, Engineering. 5 (2019) 702–720. https://doi.org/10.1016/J.ENG.2019.07.002.

[123] A. Baroutaji, A. Arjunan, A. Niknejad, T. Tran, A.-G. Olabi, Application of Cellular Material in Crashworthiness Applications: An Overview, in: Ref. Modul. Mater. Sci. Mater. Eng., Elsevier, 2019. https://doi.org/10.1016/B978-0-12-803581-8.09268-7.

[124] N.T. Aboulkhair, M. Simonelli, L. Parry, I. Ashcroft, C. Tuck, R. Hague, 3D printing of Aluminium alloys: Additive Manufacturing of Aluminium alloys using selective laser melting, Prog. Mater. Sci. 106 (2019) 100578. https://doi.org/10.1016/J.PMATSCI.2019.100578.

[125] J.N. Grima, R. Jackson, A. Alderson, K.E. Evans, Do Zeolites Have Negative Poisson's Ratios?, Adv. Mater. 12 (2000) 1912–1918. https://doi.org/10.1002/1521-4095(200012)12:24<1912::AID-ADMA1912>3.0.CO;2-7.

[126] Z. Dong, Y. Li, T. Zhao, W. Wu, D. Xiao, J. Liang, Experimental and numerical studies on the compressive mechanical properties of the metallic auxetic reentrant honeycomb, Mater. Des. 182 (2019) 108036. https://doi.org/10.1016/j.matdes.2019.108036.

[127] T. Mukhopadhyay, S. Adhikari, Effective in-plane elastic properties of auxetic honeycombs with spatial irregularity, Mech. Mater. 95 (2016) 204–222. https://doi.org/10.1016/J.MECHMAT.2016.01.009.

[128] L. Boldrin, S. Hummel, F. Scarpa, D. Di Maio, C. Lira, M. Ruzzene, C.D.L. Remillat, T.C. Lim, R. Rajasekaran, S. Patsias, Dynamic behaviour of auxetic gradient composite hexagonal honeycombs, Compos. Struct. 149 (2016) 114–124. https://doi.org/10.1016/J.COMPSTRUCT.2016.03.044.

[129] E. Harkati, N. Daoudi, A. Bezazi, A. Haddad, F. Scarpa, In-plane elasticity of a multi re-entrant auxetic honeycomb, Compos. Struct. 180 (2017) 130–139. https://doi.org/10.1016/J.COMPSTRUCT.2017.08.014.

[130] X.-C. Zhang, L.-Q. An, H.-M. Ding, X.-Y. Zhu, M. El-Rich, The influence of cell micro-structure on the in-plane dynamic crushing of honeycombs with negative Poisson's ratio, J. Sandw. Struct. Mater. 17 (2015) 26–55. https://doi.org/10.1177/1099636214554180.

[131] ISO 7500-1:2018 - Metallic materials -- Calibration and verification of static uniaxial testing machines -- Part 1: Tension/compression testing machines -- Calibration and verification of the force-measuring system, 2018. https://www.iso.org/standard/72572.html (accessed January 28, 2019).

[132] Y. Xue, X. Wang, W. Wang, X. Zhong, F. Han, Compressive property of Al-based auxetic lattice structures fabricated by 3-D printing combined with investment casting, Mater. Sci. Eng. A. 722 (2018) 255–262. https://doi.org/10.1016/J.MSEA.2018.02.105.

[133] S. Bai, N. Perevoshchikova, Y. Sha, X. Wu, The Effects of Selective Laser Melting Process Parameters on Relative Density of the AlSi10Mg Parts and Suitable Procedures of the Archimedes Method, Appl. Sci. 9 (2019) 583. https://doi.org/10.3390/app9030583.

[134] D. Buchbinder, H. Schleifenbaum, S. Heidrich, W. Meiners, J. Bültmann, High Power Selective Laser Melting (HP SLM) of Aluminum Parts, Phys. Procedia. 12 (2011) 271–278. https://doi.org/10.1016/J.PHPRO.2011.03.035.

[135] L. Thijs, K. Kempen, J.-P. Kruth, J. Van Humbeeck, Fine-structured aluminium products with controllable texture by selective laser melting of pre-alloyed AlSi10Mg powder, Acta Mater. 61 (2013) 1809–1819. https://doi.org/10.1016/J.ACTAMAT.2012.11.052.

[136] K. V. Yang, P. Rometsch, T. Jarvis, J. Rao, S. Cao, C. Davies, X. Wu, Porosity formation mechanisms and fatigue response in Al-Si-Mg alloys made by selective laser melting, Mater. Sci. Eng. A. 712 (2018) 166–174. https://doi.org/10.1016/J.MSEA.2017.11.078.

[137] C. Weingarten, D. Buchbinder, N. Pirch, W. Meiners, K. Wissenbach, R. Poprawe, Formation and reduction of hydrogen porosity during selective laser melting of AlSi10Mg, J. Mater. Process. Technol. 221 (2015) 112–120. https://doi.org/10.1016/J.JMATPROTEC.2015.02.013.

[138] V. Weißmann, P. Drescher, R. Bader, H. Seitz, H. Hansmann, N. Laufer, Comparison of Single Ti 6 Al 4 V Struts Made Using Selective Laser Melting and Electron Beam Melting Subject to Part Orientation, Metals (Basel). (2017). https://doi.org/10.3390/met7030091.

[139] A.H. Maamoun, Y.F. Xue, M.A. Elbestawi, S.C. Veldhuis, A.H. Maamoun, Y.F. Xue, M.A. Elbestawi, S.C. Veldhuis, Effect of Selective Laser Melting Process Parameters on the Quality of Al Alloy Parts: Powder Characterization, Density, Surface Roughness, and Dimensional Accuracy, Materials (Basel). 11 (2018) 2343. https://doi.org/10.3390/ma11122343.

[140] J.P.M. Whitty, F. Nazare, A. Alderson, J.P.M.; Whitty, A. Alderson, Modelling the effects of density variations on the in-plane Poisson's ratios and Young's Moduli of periodic conventional and re-entrant honeycombs-Part 1: Rib thickness variations., Cell. Polym. 21 (2002) 69. http://digitalcommons.bolton.ac.uk/cmri_journalspr/2-- (accessed September 4, 2019).

[141] K. Bari, A. Arjunan, Extra low interstitial titanium based fully porous morphological bone scaffolds manufactured using selective laser melting, J. Mech. Behav. Biomed. Mater. 95 (2019) 1–12. https://doi.org/10.1016/j.jmbbm.2019.03.025.

[142] A. Vance, K. Bari, A. Arjunan, Investigation of Ti64 sheathed cellular anatomical structure as a tibia implant, Biomed. Phys. Eng. Express. 5 (2019) 035008. https://doi.org/10.1088/2057-1976/ab0bd7.

[143] A. Vance, K. Bari, A. Arjunan, Compressive performance of an arbitrary stiffness matched anatomical Ti64 implant manufactured using Direct Metal Laser Sintering, Mater. Des. 160 (2018) 1281–1294. https://doi.org/10.1016/j.matdes.2018.11.005.

[144] S.M. Ahmadi, G. Campoli, S. Amin Yavari, B. Sajadi, R. Wauthle, J. Schrooten, H. Weinans, A.A. Zadpoor, Mechanical behavior of regular open-cell porous biomaterials made of diamond lattice unit cells, J. Mech. Behav. Biomed. Mater. 34 (2014) 106–115. https://doi.org/10.1016/j.jmbbm.2014.02.003.

[145] A.A. Zadpoor, Bone tissue regeneration: the role of scaffold geometry, Biomater. Sci. 3 (2015) 231–245. https://doi.org/10.1039/C4BM00291A.

[146] A.A. Zadpoor, Mechanics of additively manufactured biomaterials, J. Mech. Behav. Biomed. Mater. 70 (2017) 1–6. https://doi.org/10.1016/j.jmbbm.2017.03.018.

[147] B. Ellul, M. Muscat, J.N. Grima, On the effect of the Poisson's ratio (positive and negative) on the stability of pressure vessel heads, Phys. Status Solidi. 246 (2009) 2025–2032. https://doi.org/10.1002/pssb.200982033.

[148] Z. Yang, Q. Yang, G. Zhang, Poisson's ratio and Young's modulus in single-crystal copper nanorods under uniaxial tensile loading by molecular dynamics, Phys. Lett. A. 381 (2017) 280–283. https://doi.org/10.1016/j.physleta.2016.10.044.

[149] K. V Tretiakov, K.W. Wojciechowski, Orientational phase transition between hexagonal solids in planar systems of hard cyclic pentamers and heptamers, J. Phys. Condens. Matter. 14 (2002) 1261–1273. https://doi.org/10.1088/0953-8984/14/6/313.

[150] K. V. Tretiakov, K.W. Wojciechowski, Monte Carlo simulation of two-dimensional hard body systems with extreme values of the Poisson's ratio, Phys. Status Solidi. 242 (2005) 730–741. https://doi.org/10.1002/pssb.200460390.

[151] R. LAKES, Foam Structures with a Negative Poisson's Ratio, Science (80-.). 235 (1987) 1038–1040. https://doi.org/10.1126/science.235.4792.1038.

[152] G.T. Evans, Hard body model for chiral nematic liquid crystals, Mol. Phys. 77 (1992) 969–981. https://doi.org/10.1080/00268979200102911.

[153] K.E. Evans, Tensile network microstructures exhibiting negative Poisson's ratios, J. Phys. D. Appl. Phys. 22 (1989) 1870–1876. https://doi.org/10.1088/0022-3727/22/12/011.

[154] Y. Xue, W. Wang, F. Han, Enhanced compressive mechanical properties of aluminum based auxetic lattice structures filled with polymers, Compos. Part B Eng. 171 (2019) 183–191. https://doi.org/10.1016/j.compositesb.2019.05.002.

[155] J. Zhang, G. Lu, Z. Wang, D. Ruan, A. Alomarah, Y. Durandet, Large deformation of an auxetic structure in tension: Experiments and finite element analysis, Compos. Struct. 184 (2018) 92–101. https://doi.org/10.1016/j.compstruct.2017.09.076.

[156] L. Yang, O. Harrysson, H. West, D. Cormier, S. Li, H. Hassanin, M.M. Attallah, N.J.E. Adkins, K. Essa, The development of TiNi-based negative Poisson's ratio structure using selective laser melting, Acta Mater. 105 (2016) 75–83. https://doi.org/https://doi.org/10.1016/j.actamat.2015.12.017.

[157] Z.D. Sha, C.M. She, G.K. Xu, Q.X. Pei, Z.S. Liu, T.J. Wang, H.J. Gao, Metallic glass-based chiral nanolattice: Light weight, auxeticity, and superior mechanical properties, Mater. Today. 20 (2017) 569–576. https://doi.org/https://doi.org/10.1016/j.mattod.2017.10.001.

[158] R. Hedayati, M. Sadighi, M. Mohammadi-Aghdam, A.A. Zadpoor, Mechanical properties of additively manufactured octagonal honeycombs, Mater. Sci. Eng. C. 69 (2016) 1307–1317. https://doi.org/10.1016/j.msec.2016.08.020.

[159] X. Li, C. Wang, W. Zhang, Y. Li, Fabrication and compressive properties of Ti6Al4V implant with honeycomb-like structure for biomedical applications, Rapid Prototyp. J. 16 (2010) 44–49. https://doi.org/10.1108/13552541011011703.

[160] D. Kumar, A. Banerjee, Effect of heterogeneity on crushing failure of disordered staggered-square honeycombs, Compos. Struct. 240 (2020) 112055. https://doi.org/10.1016/j.compstruct.2020.112055.

[161] S. Duan, Y. Tao, H. Lei, W. Wen, J. Liang, D. Fang, Enhanced out-of-plane compressive strength and energy absorption of 3D printed square and hexagonal honeycombs with variable-thickness cell edges, Extrem. Mech. Lett. 18 (2018) 9–18. https://doi.org/10.1016/j.eml.2017.09.016.

[162] L. Zhang, B. Song, A. Zhao, R. Liu, L. Yang, Y. Shi, Study on mechanical properties of honeycomb pentamode structures fabricated by laser additive manufacturing: Numerical simulation and experimental verification, Compos. Struct. 226 (2019) 111199. https://doi.org/10.1016/j.compstruct.2019.111199.

[163] R. Hedayati, M. Sadighi, M. Mohammadi Aghdam, A.A. Zadpoor, Mechanical properties of additively manufactured thick honeycombs, Materials (Basel). 9 (2016) 613. https://doi.org/10.3390/ma9080613.

[164] K. Genovese, S. Leeflang, A.A. Zadpoor, Microscopic full-field three-dimensional strain measurement during the mechanical testing of additively manufactured porous biomaterials, J. Mech. Behav. Biomed. Mater. 69 (2017) 327–341. https://doi.org/10.1016/j.jmbbm.2017.01.010.

[165] A. Ahmed, A. Majeed, Z. Atta, G. Guozhu, Dimensional Quality and Distortion Analysis of Thin-Walled Alloy Parts of AlSi10Mg Manufactured by Selective Laser Melting, J. Manuf. Mater. Process. 3 (2019) 51. https://doi.org/10.3390/jmmp3020051.

[166] T. Yu, H. Hyer, Y. Sohn, Y. Bai, D. Wu, Structure-property relationship in high strength and lightweight AlSi10Mg microlattices fabricated by selective laser melting, Mater. Des. 182 (2019) 108062. https://doi.org/10.1016/J.MATDES.2019.108062.

[167] W.H. Kan, Y. Nadot, M. Foley, L. Ridosz, G. Proust, J.M. Cairney, Factors that affect the properties of additively-manufactured AlSi10Mg: Porosity versus microstructure, Addit. Manuf. 29 (2019) 100805. https://doi.org/10.1016/J.ADDMA.2019.100805.

[168] A. Hadadzadeh, B. Shalchi Amirkhiz, A. Odeshi, J. Li, M. Mohammadi, Role of hierarchical microstructure of additively manufactured AlSi10Mg on dynamic loading behavior, Addit. Manuf. 28 (2019) 1–13. https://doi.org/10.1016/J.ADDMA.2019.04.012.

[169] J. Chen, W. Hou, X. Wang, S. Chu, Z. Yang, Microstructure, porosity and mechanical properties of selective laser melted AlSi10Mg, Chinese J. Aeronaut. (2019). https://doi.org/10.1016/j.cja.2019.08.017.

[170] C. Yan, L. Hao, A. Hussein, S.L. Bubb, P. Young, D. Raymont, Evaluation of light-weight AlSi10Mg periodic cellular lattice structures fabricated via direct metal laser sintering, J. Mater. Process. Technol. 214 (2014) 856–864. https://doi.org/10.1016/J.JMATPROTEC.2013.12.004.

[171] M. Liu, N. Takata, A. Suzuki, M. Kobashi, Development of gradient microstructure in the lattice structure of AlSi10Mg alloy fabricated by selective laser melting, J. Mater. Sci. Technol. (2019). https://doi.org/10.1016/J.JMST.2019.06.015.

[172] N. Karnessis, G. Burriesci, Uniaxial and buckling mechanical response of auxetic cellular tubes, Smart Mater. Struct. 22 (2013) 084008. https://doi.org/10.1088/0964-1726/22/8/084008.

[173] A. Baroutaji, E. Morris, A.G. Olabi, Quasi-static response and multi-objective crashworthiness optimization of oblong tube under lateral loading, Thin-Walled Struct. 82 (2014) 262–277. https://doi.org/10.1016/j.tws.2014.03.012.

[174] A. Baroutaji, S. Lenihan, K. Bryan, Compaction analysis and optimisation of convex-faced pharmaceutical

tablets using numerical techniques, Particuology. (2019). https://doi.org/10.1016/J.PARTIC.2018.11.002.

[175] A.K. Das, S. Dewanjee, Optimization of Extraction Using Mathematical Models and Computation, Comput. Phytochem. (2018) 75–106. https://doi.org/10.1016/B978-0-12-812364-5.00003-1.

[176] A. Baroutaji, M.D.D. Gilchrist, D. Smyth, A.G.G. Olabi, Crush analysis and multi-objective optimization design for circular tube under quasi-static lateral loading, Thin-Walled Struct. 86 (2015) 121–131. https://doi.org/10.1016/j.tws.2014.08.018.

[177] L. St»hle, S. Wold, Analysis of variance (ANOVA), Chemom. Intell. Lab. Syst. 6 (1989) 259–272. https://doi.org/10.1016/0169-7439(89)80095-4.

[178] A.S. Praveen, A. Arjunan, Parametric optimisation of High-Velocity Oxy-Fuel Nickel-Chromium-Silicon-Boron and Aluminium-Oxide coating to improve erosion wear resistance, Mater. Res. Express. (2019). https://doi.org/10.1088/2053-1591/ab301c.

[179] S.L.M. Ribeiro Filho, T.A.A. Silva, L.M.G. Vieira, T.H. Panzera, K. Boba, F. Scarpa, Geometric effects of sustainable auxetic structures integrating the particle swarm optimization and finite element method, Mater. Res. 17 (2014) 747–757. https://doi.org/10.1590/S1516-14392014005000024.